Remote Sensing of Environment 112 (2008) 3012–3029

Contents lists available at ScienceDirect

Remote Sensing of Environment

journal homepage: www.elsevier.com/locate/rse

Validation of clear-sky radiances over oceans simulated with MODTRAN4.2 and global NCEP GDAS fields against nighttime NOAA15-18 and MetOp-A AVHRR data

Prasanjit Dash [a,b,*], Alexander Ignatov [a]

[a] NOAA NESDIS, Center for Satellite Applications and Research (STAR), 5200 Auth Road, Camp Springs, Maryland 20746, USA
[b] Cooperative Institute for Research in the Atmospheres (CIRA), Colorado State University, Foothills Campus, Fort Collins, Colorado 80523, USA

ARTICLE INFO

Article history:
Received 24 July 2007
Received in revised form 21 January 2008
Accepted 23 February 2008

Keywords:
RTM
RTM bias
MODTRAN
AVHRR
MetOp-A
NOAA
NCEP
Sea surface temperature
Sea surface emissivity
Fresnel
Validation
Cloud
Halos
Aerosol in TIR

ABSTRACT

An accurate and globally representative forward radiative transfer model (RTM) is needed to explore improvements in sea surface temperature (SST) retrievals from spaceborne infrared observations. This study evaluates the biases in top-of-atmosphere (TOA) brightness temperatures (BT) modeled with the moderate resolution transmission (MODTRAN4.2) band RTM, bounded by a Fresnel's reflective flat sea surface. This model is used to simulate global clear-sky Advanced Very High Resolution Radiometer (AVHRR) nighttime BTs from NOAA-15 through 18 and MetOp-A platforms for one full day of 18 February 2007. Inputs to RTM (SST fields and vertical profiles of atmospheric relative humidity, temperature, pressure, and geopotential height) are specified from the National Centers for Environmental Prediction's (NCEP) Global Data Assimilation System (GDAS) data. Model BTs in AVHRR channels 3B (3.7 μm), 4 (11 μm), and 5 (12 μm) are then compared with their respective measured counterparts, available in the NESDIS operational SST files. Ideally, the RTM should match the observations, but in fact, the modeled BTs are biased high with respect to the AVHRR BTs. The "Model minus Observation" (M − O) bias ranges from about 0 to 2 K, depending upon spectral band, view zenith angle, and sea and atmosphere state at the retrieval point. The bias asymptotically decreases towards confidently clear-sky conditions, but it never vanishes and invariably shows channel-specific dependencies on view zenith angle and geophysical conditions (e.g., column water vapor and sea–air temperature difference). Fuller exploration of the potential of the current RTM (e.g., adding global vertical aerosol profiles) or improvements to its input (NCEP SST and atmospheric profiles) may reduce this bias, but they cannot fully reconcile its spectral and angular structure. The fact that the M−O biases are closely reproducible for five AVHRR sensors flown onboard different platforms adds confidence in the validation approach employed in this study. We emphasize the need for establishing a globally adequate forward RTM for the use in SST modeling and retrievals. A first test of the RTM adequacy is its ability, when used in conjunction with the global fields from the numerical weather prediction models, to reproduce the TOA clear-sky radiances measured by satellite sensors.

© 2008 Elsevier Inc. All rights reserved.

1. Introduction

Sea surface temperatures (SST) are derived from measurements in the infrared window channels using either regression or physical algorithms. Regression-based multi-channel (MCSST) and non-linear (NLSST) techniques have been in operational use since the 1980s and 1990s, respectively, with the data from the Advanced Very High Resolution Radiometers (AVHRR) flown onboard NOAA satellites (McClain et al., 1985; Walton et al., 1998). They continue to be employed for SST retrievals from the Moderate Resolution Imaging Spectroradiometers (MODIS) flown onboard Terra and Aqua satellites (Brown & Minnett, 1999) and will also be used with the data from the Visible and Infrared Imager/Radiometer Suite (VIIRS) to be flown onboard the future National Polar-orbiting Operational Environmental Satellite System (NPOESS) (Sikorski et al., 2002). Coefficients of regression algorithms are customarily derived empirically against in-situ SSTs and sometimes theoretically using radiative transfer model (RTM) simulations (cf., Merchant et al., 1999). Physical retrieval algorithms based on solving the radiative transfer equation in each retrieval point have been also proposed (e.g., Susskind et al., 1984; Uddstrom & McMillin, 1994) but not shown to outperform the simple regression techniques, in an operational setting. Globally representative and accurate RTM, carefully validated against collocated satellite measurements, is the key to the improvements in all these SST retrieval techniques.

In this study, a forward RTM is tested based on the Moderate Resolution Transmission (MODTRAN4.2) band model (Berk et al., 2000). MODTRAN was selected for these analyses because this RTM has been long publicly available and its heritage traces back to

* Corresponding author. NOAA NESDIS, Center for Satellite Applications and Research (STAR), 5200 Auth Road, Camp Springs, Maryland 20746, USA. Tel.: +1 301 763 8053x168; fax: +1 301 763 8572.
E-mail address: prasanjit_dash@yahoo.com (P. Dash).

0034-4257/$ – see front matter © 2008 Elsevier Inc. All rights reserved.
doi:10.1016/j.rse.2008.02.013

LOWTRAN. Both RTMs have been widely used for a variety of remote sensing analyses and applications, mainly from wide-band satellite imagers. In particular, different versions of MODTRAN/LOWTRAN have been evaluated for the analyses of SST retrievals from the heritage sensors (e.g., Deschamps and Phulpin, 1980; Barton et al., 1989; Francois et al., 2002; Merchant and Le Borgne, 2004). More recently, MODTRAN4.2 has been also employed for the development of SST algorithm for the VIIRS instrument onboard the future national polar system, NPOESS (Sikorski et al., 2002).

Water vapor spectroscopy is the key for the radiative transfer in the window regions. MODTRAN4.2 uses the CKD2.4 water vapor continuum (Clough et al., 1989) and HITRAN 2000 database for lines (Rothman et al., 2003). Merchant et al. (1999) identified the need for improvement in the earlier versions of the CKD. In recent years, most RTMs have switched over to an advanced MTCKD formulation (e.g., Saunders et al., 2007). In this study, we have chosen to validate the MODTRAN4.2 RTM "as is", as an average user of this RTM would do. We believe that these validation results are of interest for a wide range of remote sensing practitioners, including those who use this RTM for SST analyses.

To satisfy the requirement of global representativeness, spectral atmospheric transmittances and upwelling and downwelling radiances are calculated using vertical profiles of relative humidity (RH), temperature (T), pressure (P), and geopotenial height (GH) specified from the National Centers for Environmental Prediction's (NCEP) Global Data Assimilation System (GDAS). Spectral emissivity for a flat surface is modeled outside MODTRAN, using Fresnel's equations and Snell's law, from the complex refractive index of water. The spectral atmospheric parameters and emissivities are calculated for a given sensor view geometry at a step of 1 cm^{-1} and substituted into the radiative transfer equation, along with the Reynolds–Smith bulk SST corrected for the skin-bulk difference using the wind speed dependent parameterization of Donlon et al. (2002). The resulting top-of-atmosphere (TOA) spectral radiances are convolved with the channel spectral response functions and converted to brightness temperatures (BT). Extraterrestrial radiation, scattering effects, and reflectance from a wind-roughened surface are not considered in the current RTM. Sensitivity to aerosols is preliminarily checked using literature review and calculations with the "navy maritime" model available in MODTRAN4.2.

The key element of this study is validation of this forward RTM against observed nighttime clear-sky AVHRR BTs obtained from the NESDIS operational SST system. The comparisons are made in three infrared (IR) channels, 3B (3.7 μm), 4 (11 μm), and 5 (12 μm), for five AVHRR/3 sensors flown onboard NOAA-15 through 18 and MetOp-A platforms, which overpass at night between approximately 9:30 pm and 5:20 am local equator crossing time. The objective is to see if the RTM simulations match the AVHRR BTs. Of particular interest to us is whether the RTM can reproduce the observed spectral, angular, and geophysical (water vapor, SST, sea–air temperature difference, wind speed) dependencies in AVHRR BTs that are critically important for SST retrievals. All analyses are performed for two types of surfaces, blackbody and flat Fresnel's reflector, to quantify the effect of emissivity on the M−O bias. Including emissivity in the RTM indeed brings it closer to the AVHRR in all bands; however, the RTM remains biased high and still does not fully reproduce the major trends in the AVHRR BTs. The magnitude of the bias is reduced towards confidently clear-sky conditions, but the discrepancy still persists. The spectral and angular structure of the bias suggests that it cannot be fully attributed to possible incompleteness of the employed RTM (e.g., missing aerosol or wind-effects) or errors in the NCEP GDAS input. Furthermore, the fact that the bias is consistent across five sensors adds confidence in its validity and calls for improvements in the forward RTM before it can be used to explore improvements in SST retrievals.

The paper is organized as follows. Section 2 describes the forward RTM, including the implementation of MODTRAN4.2 with NCEP GDAS data, and the calculation of surface emissivity. It also compares spectral emissivity modeled in this study with the results of Masuda et al. (1988) and quantifies the effect of surface emissivity on the TOA BTs as a function of view zenith angle. Section 3 introduces the RTM validation approach. It also describes the AVHRR data used here as the validation standard and the procedure to collocate them in space and time with the RTM/NCEP simulations. Section 4 analyzes the M−O biases for two surfaces (blackbody and Fresnel's), and Section 5 summarizes and concludes this study.

2. Forward radiative transfer model (RTM) and input data

Assuming that there is no extraterrestrial radiation at night, scattering in the atmosphere is negligible and sea surface is flat, the spectral TOA clear-sky IR radiance is given as:

$$R^{\mathrm{TOA}}(i,\theta) = \underbrace{\varepsilon(i,\theta)\cdot B(i,T_{\mathrm{sfc}})}_{\text{surface}}\cdot \underbrace{\tau^{\uparrow}(i,\theta)}_{\text{atmosphere}} + \underbrace{L^{\uparrow}(i,\theta)}_{\text{atmosphere}} + \underbrace{(1-\varepsilon(i,\theta))}_{\text{surface}} \times \underbrace{L^{\downarrow}(i,\theta)\cdot\tau^{\uparrow}(i,\theta)}_{\text{atmosphere}} \tag{1a}$$

Here, θ is the view zenith angle (measured at the surface), 'i' denotes wavenumber interval (1 cm^{-1}, as determined by the MODTRAN4.2 band model, Berk et al., 1998), T_{sfc} is the skin SST, ε is the surface emissivity, B is the Planck radiance, $\tau^{\uparrow}$ is the atmospheric transmittance in the forward direction, and $L^{\uparrow}$ and $L^{\downarrow}$ are the atmospheric upwelling and downwelling radiances, respectively. The origin of each term is annotated below the braces.

The TOA spectral radiances computed at 1 cm^{-1} interval using Eq. (1a) are convolved with the relative spectral response (RSR, or Φ_i, also digitized at a step of 1 cm^{-1}) to calculate the TOA radiance in a sensor channel:

$$R^{\mathrm{TOA}}_{\mathrm{channel}}(\theta) = \sum_{i=\nu_1}^{\nu_2} R^{\mathrm{TOA}}(i,\theta)\cdot\Phi_i \Big/ \sum_{i=\nu_1}^{\nu_2}\Phi_i \tag{1b}$$

The RSRs (normalized at $\mathrm{RSR}_{\max}=1$) are available in Goodrum et al., 2003 (for NOAA-15 to -18) and in ITT, 2007 (for MetOp-A). (They have been also summarized at http://www.star.nesdis.noaa.gov/smcd/spb/

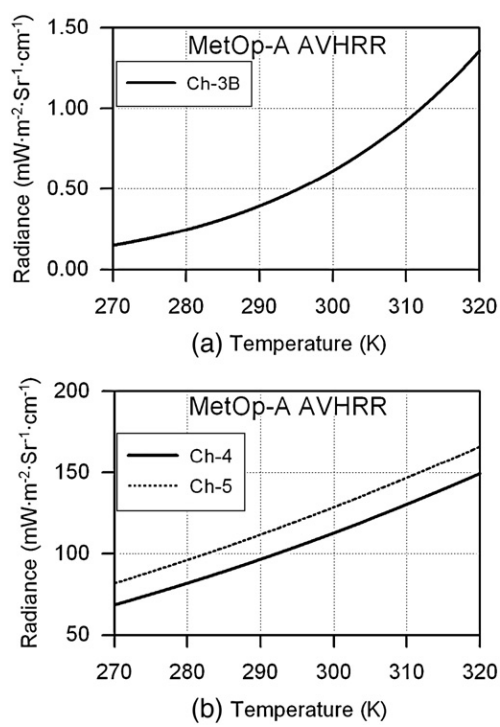

Fig. 1. Temperature to radiance conversion look-up tables for MetOp-A AVHRR channels (top) 3B; (bottom) 4 and 5.

fwu/solar_cal/spec_resp_func/index.html.) For computational simplifications in this study, all RSRs have been re-normalized to a unit area, i.e., $\sum_{i=1}^{10} \Phi_i = 1$.

Finally, the TOA BTs are calculated by linear interpolation between the two nearest grids of the temperature-to-radiance conversion look-up tables (cf., Steyn-Ross et al., 1992) pre-calculated at a step of 5×10^{-4} K. As an example, Fig. 1 plots look-up tables for AVHRR onboard MetOp-A. This procedure provides accurate BTs which are consistent with those provided by the operational AVHRR calibration procedures (Goodrum et al., 2003) to within ~ 10^{-4} K.

In Eq. (1a), the atmospheric terms, $L^{\uparrow}$, $L^{\downarrow}$, and $\tau^{\uparrow}$ are calculated with MODTRAN4.2 using profiles of RH, T, and GH specified from the NCEP GDAS files. Section 2.1 below provides more details on the GDAS data used in this study. On an implementation note, calculations of $L^{\downarrow}$ requires view angle at the surface, θ, as input, whereas calculations of $L^{\uparrow}$ and $\tau^{\uparrow}$ with MODTRAN require look angle, θ_L, at the sensor level. The two angles are related as: $\theta_L = [180° - \sin^{-1}(\sin\theta\,(R/R+H))]$, where R is the radius of the earth and H is the satellite height. Spectral emissivity values are also calculated at the same spectral step of 1 cm^{-1} as in MODTRAN4.2. Section 2.2 describes the emissivity calculation algorithm and quantifies the effect of emissivity on the TOA BTs.

2.1. NCEP GDAS data and minor gases

The National Weather Service's National Centers for Environmental Prediction (NCEP; http://www.ncep.noaa.gov/) operationally generate the Global Data Assimilation System (GDAS) gridded binary files four times daily (at 00, 06, 12, and 18 UTC) with 1° latitude–longitude resolution (181×360). More information is available at http://www.arl.noaa.gov/ss/transport/gdas1.html. In this work, five GDAS files were used: four for 18 February 2007 (00, 06, 12, 18 UTC) and one for 19 February 2007 (00 UTC). Each file reports atmospheric profiles of RH, T, and GH at 26 fixed pressure levels: P=1000, 975, 950, 925, 900, 850, 800, 750, 700, 650, 600, 550, 500, 450, 400, 350, 300, 250, 200, 150, 100, 70, 50, 30, 20, and 10mb. Additionally, pressure at the surface (P_{sfc}), near-surface T_{air} and RH, and 10m u- and v-wind components are also available. The RH values are only available up to 100 mb. To match T and GH data above 100 mb, RH values have been extrapolated to missing levels. This was achieved by calculating water densities at 150 mb and 100 mb levels, from RH and T, extrapolating them to missing layers assuming exponential decrease with height, and then converting the extrapolated water densities back to RH using level-specific values of T.

Table 1A–C in the Appendix lists optical thicknesses of all optically active gases for five AVHRR/3 sensors onboard NOAA15-18 and MetOp-A platforms and Table 2 lists their respective column integrated amounts for the six standard atmospheres (WMO, 1986) available in MODTRAN. Water vapor is the major and most variable absorbing gas in all three AVHRR bands, with continuum absorption dominating at 11 and 12 μm and line absorption prevailing at 3.7 μm. In this study, its total amount and vertical structure were specified from the NCEP GDAS files, whereas for all other gases the standard mid-latitude summer atmosphere was used. The only exception was made for CO_2, whose volume mixing ratio was increased to 385 ppmv from the mid-latitude summer default value of 330 ppmv, to account for global increase in CO_2 since the time when the standard

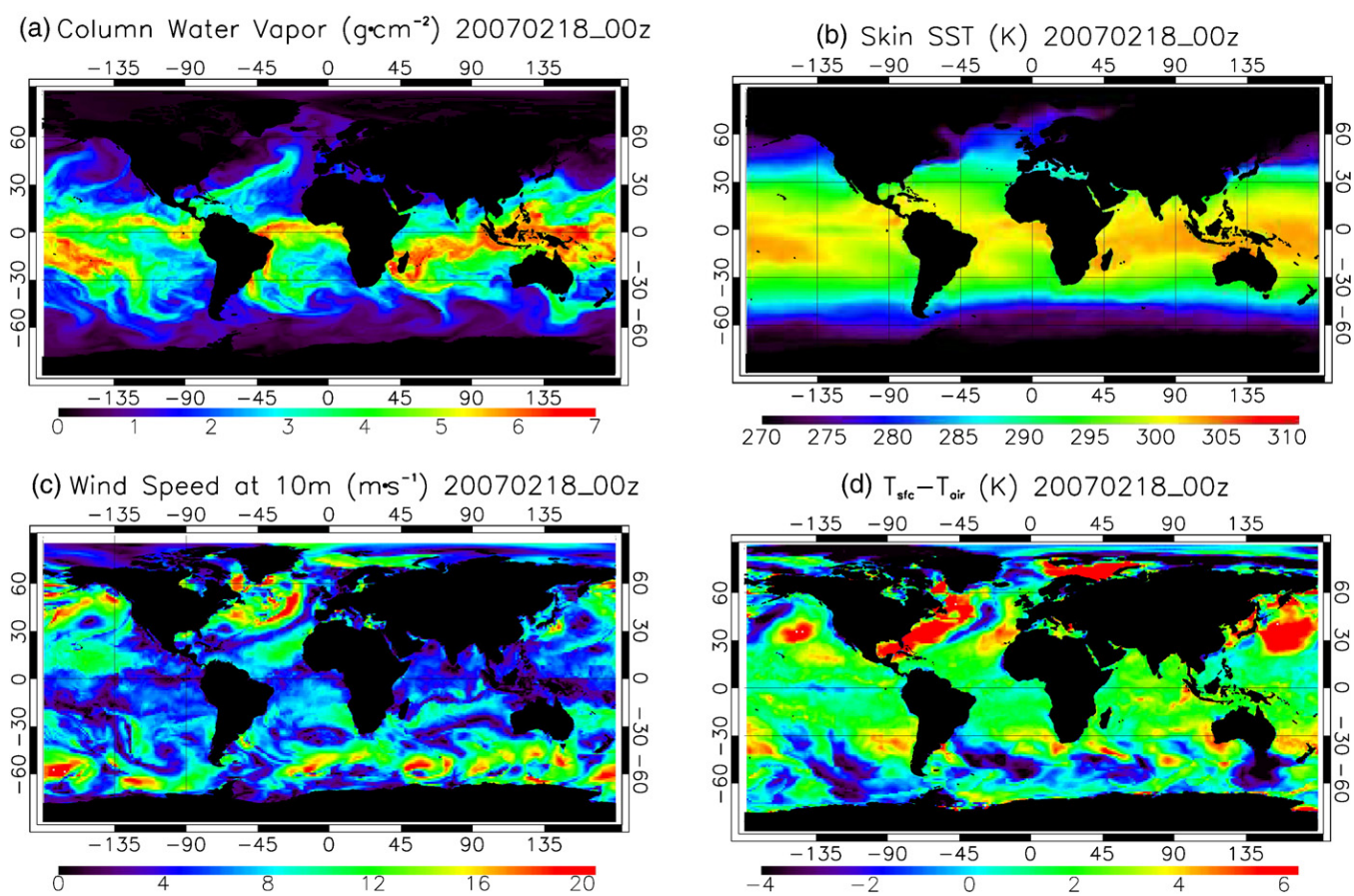

Fig. 2. Distribution, over global oceans, of key atmospheric and surface parameters on 18 February 2007 00 UTC. (a) Total column water vapor calculated from NCEP T, RH, and GH profiles. (b) Skin SST calculated from bulk Reynolds-Smith v.2 SST using parameterization of Donlon et al., 2002. (c) Wind speed at 10-m height, and (d) sea–air temperature difference. (Note that all distributions shown here are representative of all-sky conditions whereas SST retrievals and RTM validation described in this study are only performed under clear skies.)

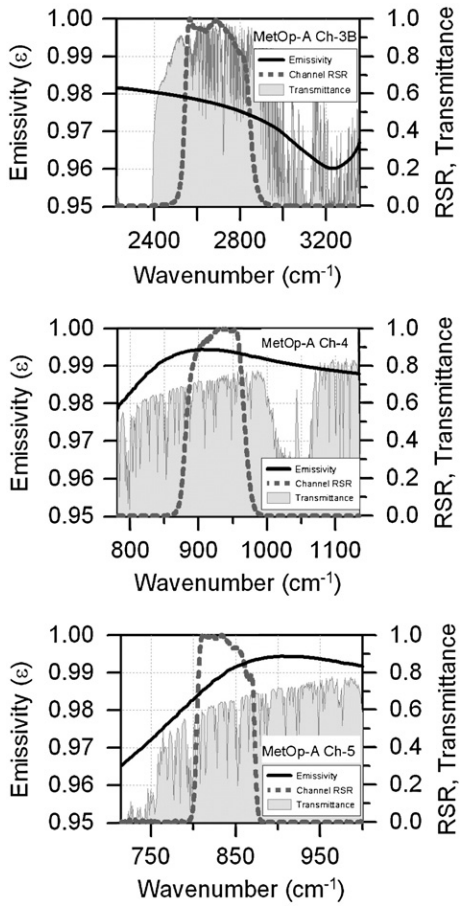

Fig. 3. Spectral emissivity of water at a step of 1 cm^{-1} within AVHRR channels (top) 3B, (middle) 4, and (bottom) 5 for nadir view (θ=0°). For reference, corresponding relative spectral responses (RSR) of MetOp-A AVHRR and nadir spectral transmittances for mid-latitude summer are annotated.

atmospheres used in MODTRAN were established. The combined effect of standard model trace gases on TOA BTs for different channels and atmospheres is shown in Table 3 in the Appendix.

Fig. 2 illustrates some key environmental variables in NCEP GDAS files over global oceans used as input to MODTRAN calculations for one fixed time on 18 February 2007 at 00 UTC. Fig. 2a shows column water vapor W (g cm^{-2}) which was calculated for each 1° grid cell by integrating the H_2O density profiles (which, in turn, were calculated from the RH, T, and GH profiles), assuming a fixed exponential decay within each layer bounded by two levels. Note that W varies within a day (figures not shown), following diurnal cycles in the RH and T atmospheric profiles as captured in the six-hourly GDAS files. The optimally interpolated Reynolds–Smith version 2 bulk SST (Reynolds et al., 2002), reported in the GDAS files as a "moving average" over a period of seven days and refreshed daily, has no diurnal cycle. However, the skin SST (shown in Fig. 2b) changes at a 6 hour interval following the diurnal variations in GDAS wind speed (shown in Fig. 2c). Skin SST is derived from the Reynolds–Smith bulk SST by applying a wind speed dependent correction by Donlon et al. (2002) given as: $T_{skin}=T_{bulk}-0.14-0.30\times\exp(-V/3.7)$, where V is wind calculated as $V=\sqrt{(u^2+v^2)}$. Corresponding global distribution of the sea–air temperature difference is also shown in Fig. 2d.

2.2. Spectral surface emissivity for a flat surface and its effect on TOA BTs

Assuming that the surface is flat, emissivity is calculated using the classical Fresnel's equations (e.g., Wu and Smith 1997; Hanafin and Minnett 2005), which are also reproduced below to facilitate the discussion in this section:

$$\varepsilon = 1 - \left[\frac{\rho_H + \rho_V}{2}\right], \text{where } \rho_H = \left[\frac{\mathbf{n}_a \cos\theta - n_w \cos\boldsymbol{\theta}_r}{\mathbf{n}_a \cos\theta + n_w \cos\boldsymbol{\theta}_r}\right]^2,$$
$$\rho_V = \left[\frac{\mathbf{n}_a \cos\boldsymbol{\theta}_r - \mathbf{n}_w \cos\theta}{\mathbf{n}_a \cos\boldsymbol{\theta}_r + \mathbf{n}_w \cos\theta}\right]^2 \quad (2)$$

Here, ρ_H and ρ_V are horizontally and vertically polarized reflection coefficients calculated from the complex refractive indices of air ($\mathbf{n}_a$) and water ($\mathbf{n}_w$). Symbols in bold denote complex numbers (i.e., $\mathbf{n}=n+i\cdot n'$, where n is real and n' imaginary part of the refractive index), and θ and $\boldsymbol{\theta}_r$ are the angles of incidence and refraction related via Snell's law, $\mathbf{n}_a\cdot\sin\theta=\mathbf{n}_w\cdot\sin\boldsymbol{\theta}_r$. All calculations in Eq. (2) are performed using complex arithmetic so that, for instance, the angle of refraction, $\boldsymbol{\theta}_r$, is formally treated as a complex number, too. In this study, $\mathbf{n}_w$ was specified with respect to air, i.e., $\mathbf{n}_w \equiv \mathbf{n}_w / \mathbf{n}_a$ and $\mathbf{n}_a$ in Eq. (2) was thus set to 1.

There are several published results on spectral refractive index of water (e.g., Hale & Querry, 1973; Downing & Williams, 1975; Segelstein, 1981). This study uses Segelstein's $\mathbf{n}_w$, which are readily available in a digital format from http://reflib.wikispaces.com. Spectral and angular emissivities, ε (i, θ), were calculated at the reference wavelengths and then interpolated to an interval of 1cm^{-1} and stored in platform- and band-specific two-dimensional look-up tables, for 3 spectral intervals covering the AVHRR/3 bands (i=3B, 4, 5) and for 17 incident angles (secθ=1 to 3 in step of 0.125). Fig. 3

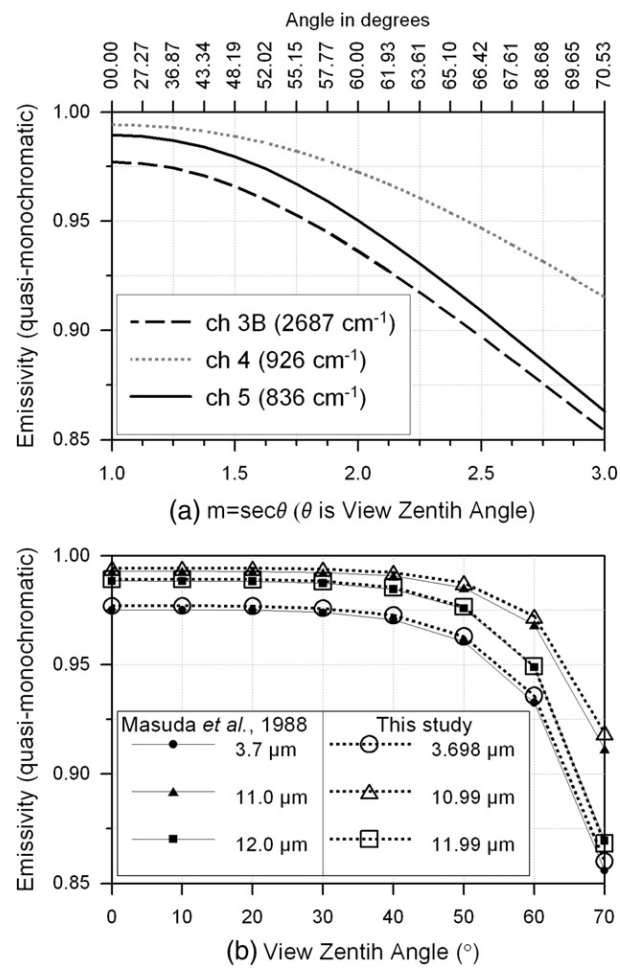

Fig. 4. (Top) Angular dependence of monochromatic sea surface emissivities for wavenumbers representative of AVHRR channels centers 3B (2687 cm^{-1}), 4 (926 cm^{-1}), and 5 (836 cm^{-1}). (Bottom) Comparison of emissivities modeled in this study versus corresponding results of Masuda et al. (1988).

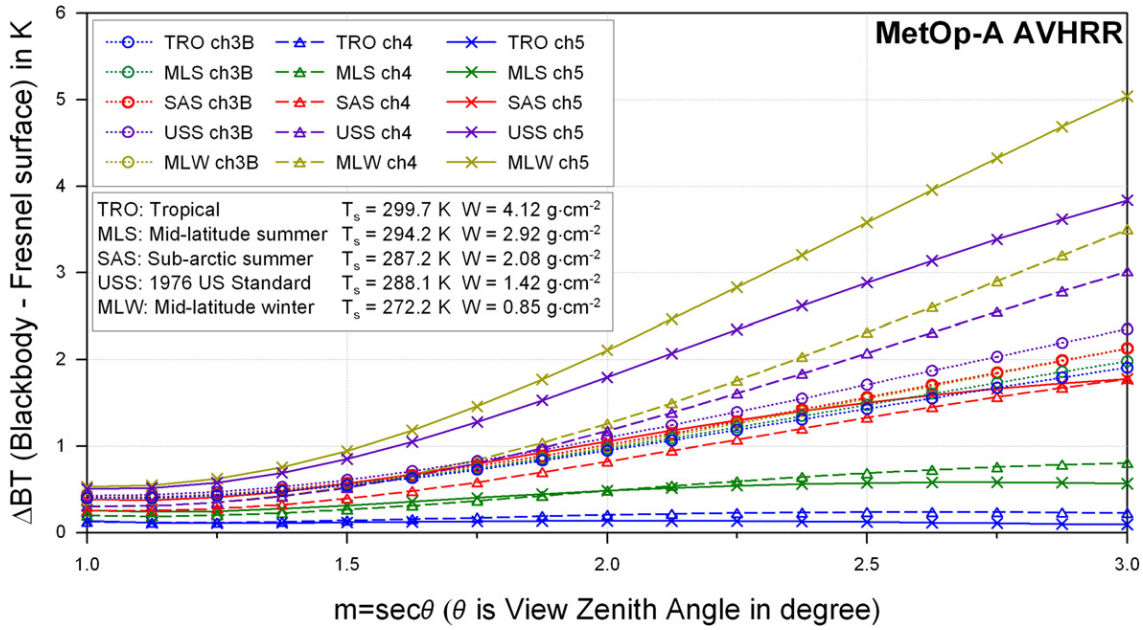

Fig. 5. Difference in TOA BT between emissive and blackbody surface, BT(ε=1)−BT(ε=Fresnel's), for five model atmospheres and three channels of MetOp-A AVHRR. (Note that the sub-arctic winter standard atmosphere was omitted, due to its low surface temperature value of 257.2 K, which is unrealistic for SST).

illustrates spectral dependence of emissivity at normal incidence, ε (i, 0). The surface is least reflective (closest to blackbody) in the 11-μm band and most reflective in the 3.7-μm band, with the 12-μm band falling in between the two. Note that the emissivity significantly changes within a given band and using a band-average emissivity is not fully accurate. In this study, TOA spectral radiances have been convolved with the RSRs following Eqs. (1a) and (1b).

Fig. 4a plots three monochromatic emissivities representative of AVHRR band centers as a function of view angle. Recall that for the AVHRR, view angle at the surface can reach approximately 68° at the edge of the scan. However, the AVHRR data used in this study are from the heritage SST system at NESDIS, which only processes data with θ<54°, where amplitude of emissivity variations with view angle is much smaller than for the full swath. As a quick test, Fig. 4b compares our calculations of emissivity with the corresponding values from Masuda et al. (1988) for a flat Fresnel's surface. Close agreement between the two results at the three quasi-monochromatic wavenumbers representative of AVHRR band centers adds confidence in the newly calculated spectral values for the full bands.

Fig. 5 shows the effect of emissivity on TOA BTs in different AVHRR channels. TOA BTs are colder for a reflective surface than for a blackbody surface, with the magnitude of the differences depending upon atmosphere and spectral interval.

To facilitate interpretation of these observations from Fig. 5, Eq. (1a) can be rewritten as (note that the spectral index, i, is omitted here, for brevity):

$$R^{\mathrm{TOA}}(\theta) = \left[B(T_{\mathrm{sfc}}) - \left(B(T_{\mathrm{sfc}}) - L^{\downarrow}(\theta)\right)(1-\varepsilon(\theta))\right] \cdot \tau^{\uparrow}(\theta) + L^{\uparrow}(\theta) \tag{3}$$

Recall that Fig. 5 was calculated assuming the atmosphere is horizontally uniform, so that the downwelling radiance, $L^{\downarrow}$, comes from a cloud-free atmosphere and $L^{\downarrow}$<B. The cold bias in TOA BT in Fig. 5 is smaller in less transparent bands and under moist atmospheres (e.g., Smith et al., 1996). In reality, however, the downwelling direction may be obstructed by a near-surface warm cloud which blocks the cold downwelling radiance and reemits at its own temperature which is much closer to SST. This is a likely scenario even though the upwelling direction is completely cloud free. In this case, $L^{\downarrow} \sim B$ and the surface appears as it is black. As a result, the TOA BT differences shown in Fig. 5 are driven even further closer to zero. Thus, in reality, the surface radiance is bracketed by two models: Fresnel's, with $L^{\downarrow}$ calculated assuming that down-welling direction is clear-sky, and black-surface model, if the downwelling direction is blocked by a warm, thick cloud. In this study, both surface models are considered and validated against AVHRR radiances.

Table 1
Mean and root-mean-squared deviation (RMSD) M−O biases for three channels of five AVHRRs derived from grids with NOBS≥8

AVHRR/ platform	Bias (model−observation)			Root mean square difference			# of collocated RTM/AVHRR grids (% total)	# of selected grids (NOBS≥8) for Bias and RMSD statistics here
	Ch-3B	Ch-4	Ch-5	Ch-3B	Ch-4	Ch-5		
MetOp-A	1.07*	−0.01	0.65	0.53	0.63	0.65	10827 (16%)	1778
NOAA-18	0.65	0.03	0.94*	0.55	0.68	0.69	11691 (15%)	1706
NOAA-17	0.61	−0.10	0.67	0.54	0.65	0.69	11194 (17%)	1912
NOAA-16	0.09*	−0.02	1.06*	0.53	0.55	0.59	8067 (18%)	1492
NOAA-15	0.75	0.15	0.85	0.61	0.59	0.63	11207 (21%)	2401
Average	0.67	0.01	0.72	0.55	0.62	0.65	10597 (17%)	1859

Also shown are: total number of grids, number of grids with NOBS≥8, and percent to total. Last row shows band-representative M−O statistics calculated by averaging individual values from different platforms. (*The out of family M−O biases for MetOp-A and NOAA-16 AVHRR channel 3B, and NOAA 16 and 18 channel 5 were not included in the average statistics.) Adding aerosols to the forward model will further reduce the biases (Section 4.5).

One of the anonymous reviewers of this manuscript suggested recalculating our emissivity look-up tables using the newer $\mathbf{n}_w$ data and including effects of salinity, temperature and wind speed on the surface emissivity. This is a valid wish which however goes far beyond our initial objective to quickly estimate the effect of surface reflectance on RTM validation. Recall also that to date, there is no consensus in the SST community on what $\mathbf{n}_w$ data should be used, and the effects of temperature and salinity on $\mathbf{n}_w$ have not been fully characterized yet in the thermal IR windows (Friedman, 1969; Pinkley et al., 1977; Masuda et al., 1988; Watts et al., 1996; Newman et al., 2005; Hanafin and Minnett, 2005; Masuda, 2006). Effect of wind speed is more complex and it is discussed later in Section 4.3. We believe, however, that a major challenge lies not in an accurate calculation of the surface emissivity, but rather in its use in the radiative transfer equation in conjunction with the downwelling atmospheric radiance which is highly uncertain in each retrieval point. The reality falls somewhere between the black and Fresnel's models, and our analyses below are aimed at better quantifying this proportion.

3. Forward model validation against AVHRR observations

Often, an RTM is evaluated via comparison against another reference RTM, such as a well established line-by-line model (cf., Anderson et al., 2007; Merchant & Le Borgne, 2004; Garand, 2003). This study explores a different validation approach whereby global

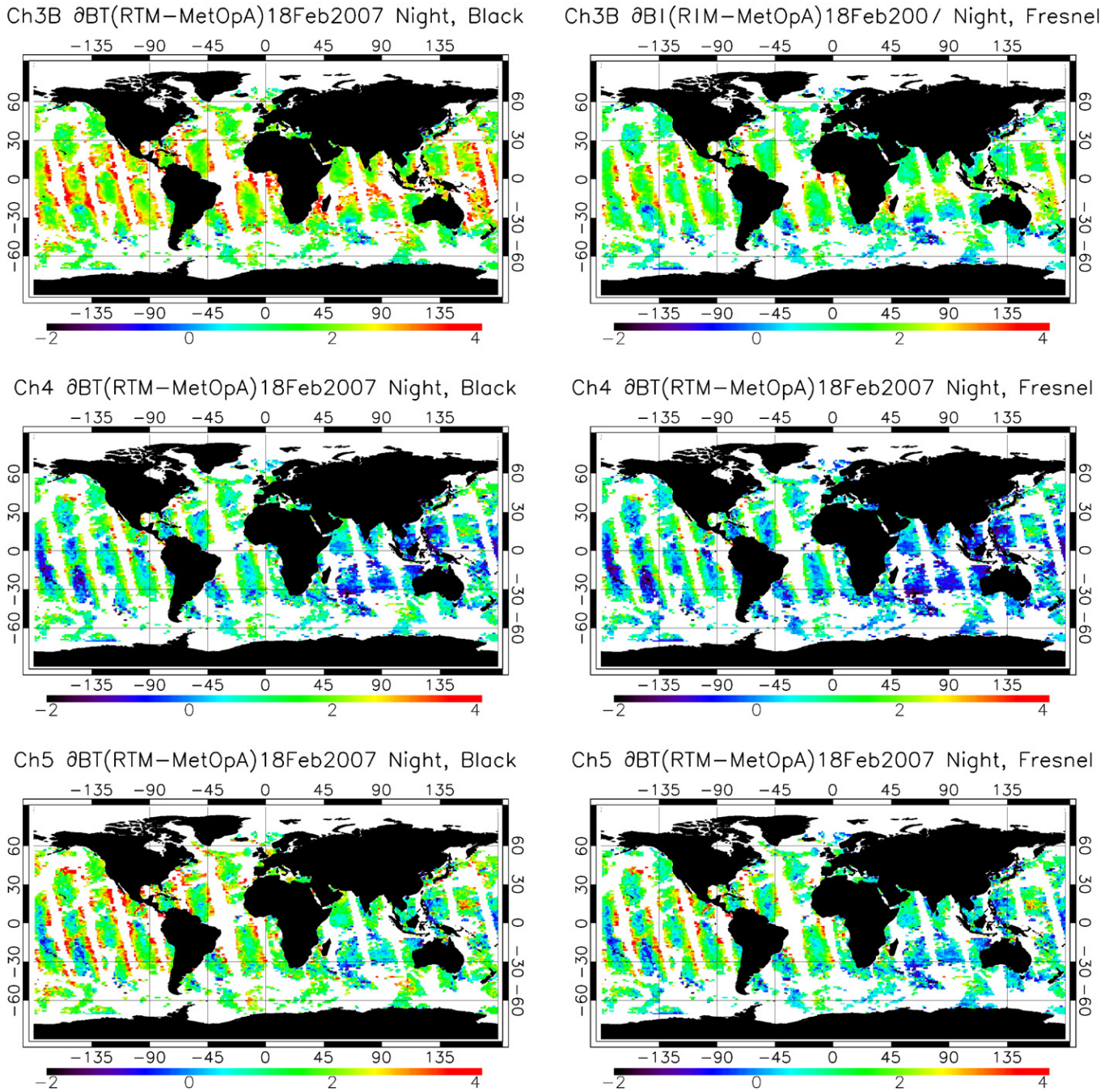

Fig. 6. Nighttime "Model−Observation" (M−O) biases in MetOp-A AVHRR channels 3B, 4, and 5 on 18 February 2007. Left panel: black surface; right panel: Fresnel's surface. Land mask is rendered in black and areas with no AVHRR data in white. Note that the RTM tends to be biased high with respect to AVHRR in all channels. The biases show zonal trends and increase towards the edge of the scan. Biases are smaller for Fresnel's than for black surface.

RTM simulations are compared against measured TOA BTs (e.g., Morcrette, 1991; Uddstrom & McMillin, 1994). The following two subsections describe the reference AVHRR data used in this study as the validation standard and the match-up procedure used to collocate the two data sets in space and time.

3.1. AVHRR data from the NESDIS heritage SST system

NESDIS has been generating operational SST products since the 1980s employing MCSST and NLSST equations (McClain et al., 1985; Walton et al., 1998) within a complex software system called the Main Unit Task (MUT). Resulting SST products are reported in rotated SST observation (SSTOBS) files, one per platform. At each given point in time, an SSTOBS file contains retrievals during the last eight days (approximately representing the full repeat cycle of a NOAA satellite). The files are renewed automatically, four times a day, around 0100, 0700, 1300, and 1800 EST. Along with SST, the SSTOBS files also report corresponding channel BTs and daytime reflectances, view zenith angles θ, solar zenith angles θ_S, UTC times, and latitude and longitude of each pixel. Global MUT processing is based on 2×2 GAC pixel arrays, resulting in an effective ~8 km resolution of SSTOBS pixel. A brief description of the NESDIS MUT system and products is given in Ignatov et al. (2004).

AVHRR nighttime BTs in channels 3B, 4, and 5 were extracted from the respective SSTOBS files for NOAA 15 through 18 and MetOp-A platforms from 00 UTC 18 February through 00 UTC 19 February, 2007.

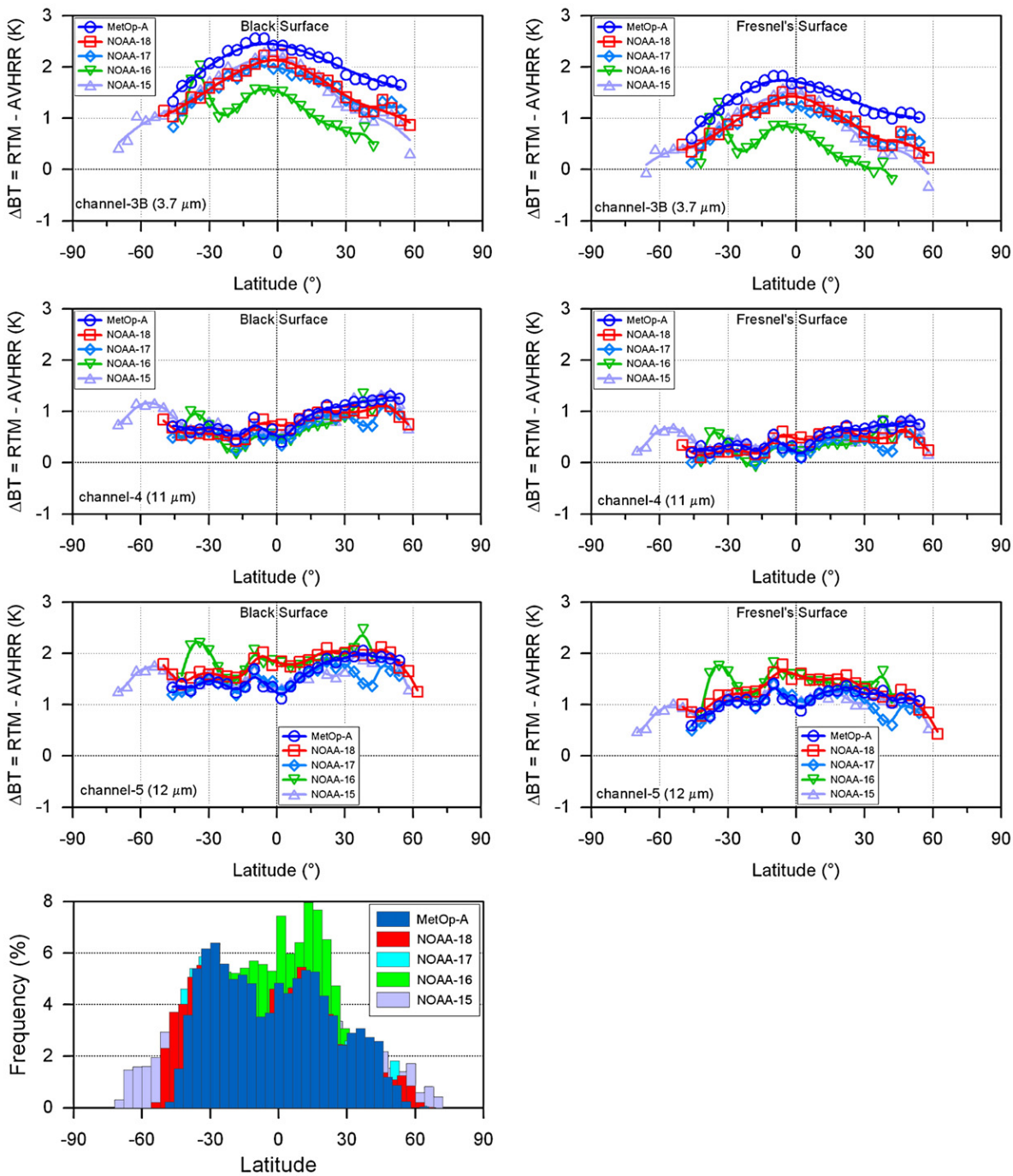

Fig. 7. Zonal distribution of the nighttime M−O biases in three AVHRR channels for NOAA 15–18 and MetOp-A on 18 February 2007 (latitude binned at 4°). Left panel: black surface; right panel: flat Fresnel's surface. Corresponding frequency distributions are also shown. (Note that trends may not be fully reliable in scarcely populated high latitudes).

Note that as of the time of this writing, only two SST products, from NOAA-18 (nighttime local equator crossing time around 2:00 am) and MetOp-A (around 9:30 pm), are considered operational at NESDIS. Three other platforms — NOAA-15 (~5:15 am), -16 (~4:00 am), and -17 (~10:00 pm)—are in a back-up mode. However, SSTOBS files are routinely generated from all five platforms and were used in the analyses below.

For the purposes of this study, nighttime pixels were defined as those with sun angle $\theta_S > 118°$. This threshold corresponds to a platform crossing between the daylight and dark and was set in an attempt to avoid data with solar contamination of the AVHRR calibration system (Cao et al., 2001). For NOAA-15 this threshold resulted in a large loss of data and was relaxed to $\theta_S > 90°$. Note that the $\theta_S = 118°$ threshold, recommended by Cao et al., relates to the sub-satellite point, whereas the MUT system provides θ_S at the pixel. Using pixel θ_S may result in an overly conservative screening on the "anti-solar" side of the swath, whereas on the "solar" side of the orbit, the screening may be insufficiently conservative and could result in residual solar contamination of the AVHRR BTs. It will be shown later that such residual contamination was indeed observed in the BTs from at least one platform, NOAA-16.

3.2. Spatial and temporal collocation of modeled and AVHRR BTs

As a first step, 8-km resolution SSTOBS nighttime BTs and corresponding solar and satellite zenith angles and UTC times from NOAA

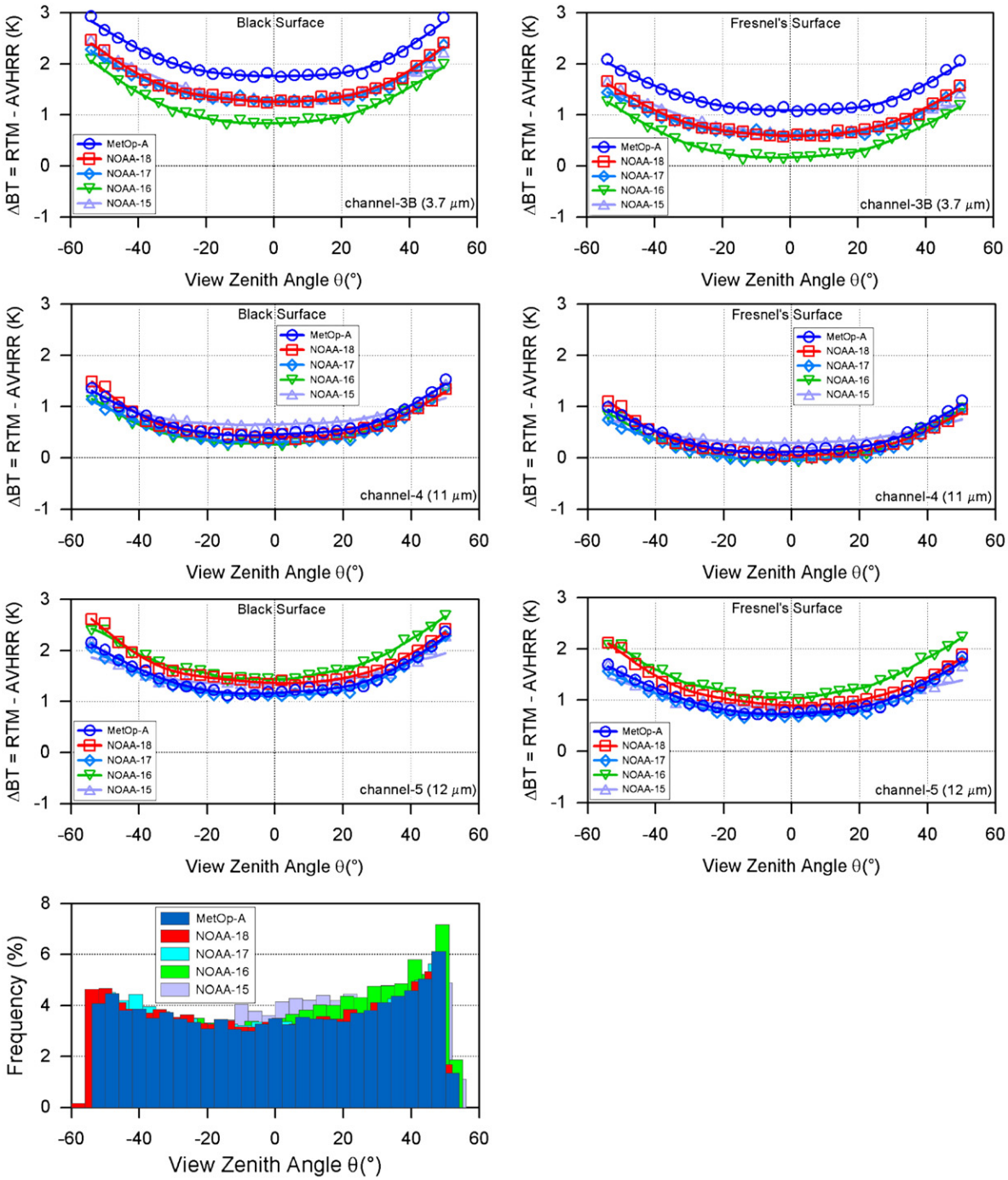

Fig. 8. Same as in Fig. 7 but as a function of view zenith angle (θ binned at 4°). Note that, accounting for aerosols or increasing amount of other absorbers will decrease the biases and their angular amplitude in proportion to ~sec θ.

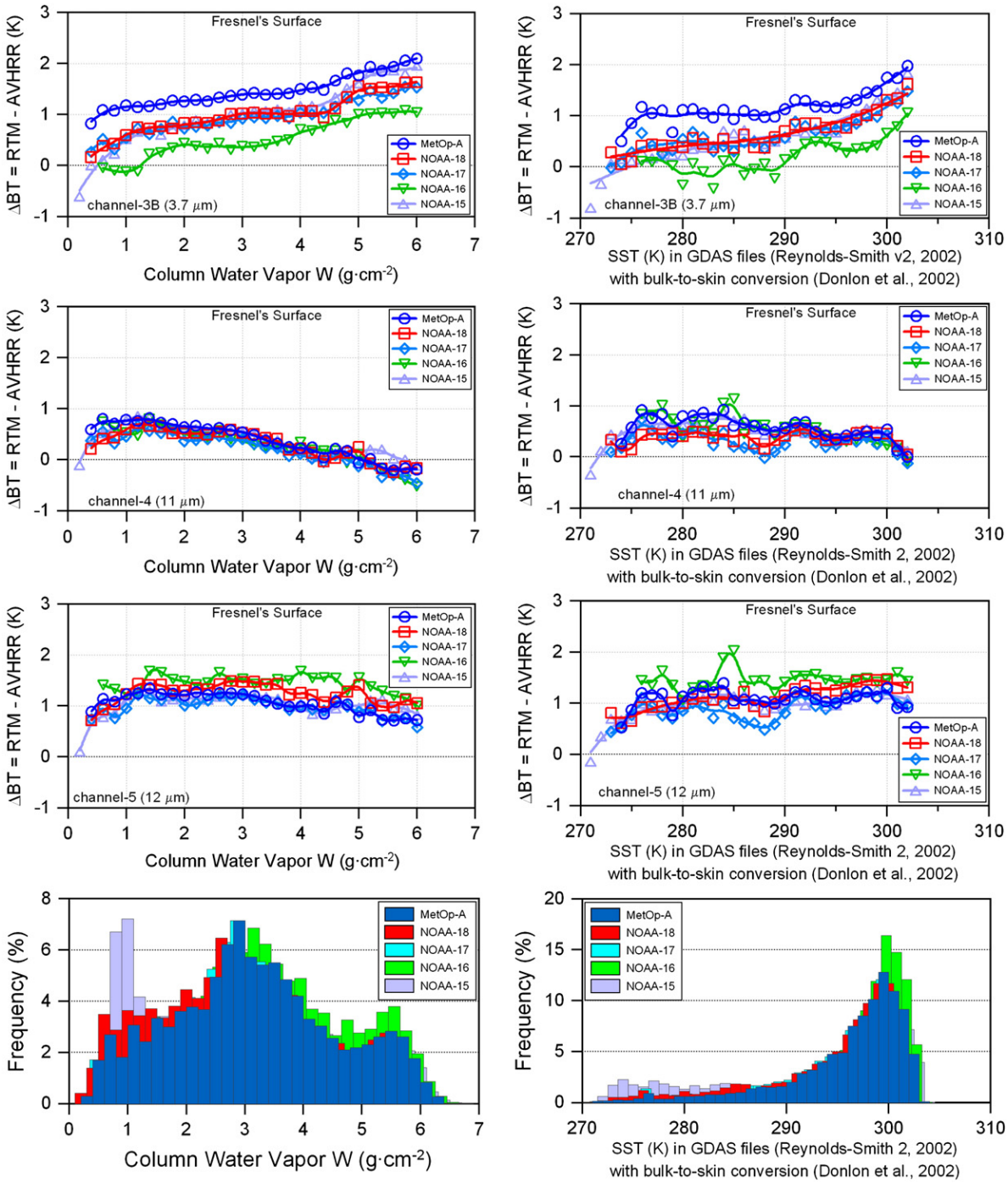

Fig. 9. Same as in Fig. 7 but as a function of (left) column water vapor (W; binned at 0.2 g cm^{-2}); and (right) sea surface temperature (SST; binned at 1 °C). Only Fresnel's surface results are shown.

15–18 and MetOp-A on 18 February 2007 were averaged into 1°×1° grid cells to match the GDAS spatial resolution. This results in approximately 10,000 "coincident model-observation data points" per platform (Table 1). The number of observations within each 1° grid cell (NOBS) was also saved to allow analyses of the effect of residual and ambient cloud on the M−O bias. Note that cloud amount parameter is not available on SSTOBS files, but one can reasonably expect that it is approximately inversely proportional to NOBS. These cloud analyses are reported in Section 4.

Next, TOA BTs have been simulated using Eq. (1a) for the corresponding average AVHRR view zenith angle. When the AVHRR θ did not match the emissivity look-up table grid, a linear interpolation was performed between the two nearest grids in secθ scale. Calculations of $L^{\downarrow}$, $L^{\uparrow}$, and $\tau^{\uparrow}$ were performed for five NCEP GDAS files from 18 February 00 UTC through 19 February 00 UTC and linearly interpolated between the two closest GDAS times, to match the AVHRR pixel observation time.

4. Analysis of the model–observation bias

In this section, the M−O bias is documented and analyzed. Errors in RTM, NCEP fields, AVHRR data, and RTM/AVHRR space–time

mismatch contribute to the bias, which can be schematically approximated as (cf., Merchant & Le Borgne, 2004):

$$E_{\mathrm{TOTAL}} = \underbrace{E_{\mathrm{RTM}} + \frac{\partial E}{\partial E_k} E_\kappa}_{\text{RTM Engine + Parameters}} + \underbrace{\frac{\partial E}{\partial E_{\mathrm{sfc}}} E_{\mathrm{sfc}} + \frac{\partial E}{\partial E_{\mathrm{atm}}} E_{\mathrm{atm}}}_{\text{RTM Input Error}} + \underbrace{\frac{\partial E}{\partial E_l} E_l + \frac{\partial E}{\partial E_t} E_t}_{\text{Collocation Error}} + \underbrace{\frac{\partial E}{\partial E_{\mathrm{RSR}}} E_{\mathrm{RSR}} + \frac{\partial E}{\partial E_{\mathrm{CAL}}} E_{\mathrm{CAL}} + \frac{\partial E}{\partial E_{\mathrm{CLD}}} E_{\mathrm{CLD}}}_{\text{AVHRR Error}} \quad (4)$$

Here, the RTM error is split into inherent E_{RTM} (RTM engine and set of radiative transfer calculation equations, such as the MODTRAN band model and Fresnel's flat surface reflectance model) and tunable E_k (RTM parameters, such as the spectral absorption coefficients calculated in MODTRAN4.2 from the HITRAN 2000, Rothman et al., 2003, or the CKD2.4 parameterization of H_2O continuum in the 10–13 μm region, Clough et al., 1989). The errors in input data include errors in SST and wind speed used for bulk-to-skin SST conversion and atmospheric variables (V_{atm}=T, RH, P, GH and missing aerosols, including assumptions of their vertical stratification). The collocation error is represented by space–time mismatches between AVHRR and NCEP data, t and l. Error in AVHRR data comes from errors in channel relative spectral response (E_{RSR}), sensor calibration (E_{CAL}), and residual cloud contamination and potential humidity halos around clouds in AVHRR clear-sky radiances (E_{CLD}).

In this study, we attempt to isolate individual components of errors in Eq. (4). The ultimate objective is to quantify the RTM component of the bias as a function of those observational conditions that are critically important for SST retrievals. In what follows, we concentrate on those features in the bias that are reproducible between different platforms and, therefore, are likely due to RTM causes (although some may come from the inaccuracies in GDAS input to RTM). As seen later in this section, biases are generally consistent across platforms and show smooth behavior as a function of governing variables. Residual cross-platform "noise" is present because one day of global data may not be sufficient to beat down the noise, and because different platforms and bins may look at slightly different global sub-samples, thus contributing to some spurious cross-platform variability in the bias.

4.1. Geographical distribution of the bias

The global distribution of the M−O biases in three AVHRR bands onboard MetOp-A is shown in Fig. 6 for black and Fresnel's surfaces. In all cases, the RTM tends to be biased warm compared to the AVHRR. Including emissivity is expected to improve RTM and reduce the bias and Fig. 6 confirms that this is indeed the case.

Fig. 7 shows zonal distributions of the biases along with zonal density plots.

The most prominent feature of Fig. 7 is overall excellent cross-platform consistency of the zonal distribution of the bias in all channels and for both surface types, with only two major exceptions, as described below.

First, channels 3B on NOAA-16 and MetOp-A fall off the main cluster formed by the other three platforms: NOAA-16 is biased −0.6K cold and MetOp-A is biased +0.4K warm. (Note that there are also similar off-cluster patterns for NOAA-16 and -18 in channel 5, though of much smaller magnitudes.) These anomalies may have been caused by the uncertainties in the spectral response functions and/or calibrations of the respective AVHRR instruments. The AVHRR instrument onboard NOAA-16 was the first in the AVHRR/3 series characterized by its manufacturer, ITT, and the reported spectral response functions may have been thus more prone to error. The MetOp-A anomaly, on the other hand, was unexpected. Efforts were made to independently verify this MetOp-A 3B out-of-family pattern, but as of the time of this revision, its cause remains unknown to us.

Another off-cluster feature is a 0.5 to 1.0 K "bump" in the NOAA-16 bias around 35°S. This feature is observed in all three AVHRR bands. Off-line analyses have shown that this bump is due to a corresponding "hump" in the AVHRR BTs, which occurs when NOAA-16 crosses the terminator and the corresponding AVHRR calibration coefficients experience large unphysical variations due to solar impingement on its blackbody (Cao et al., 2001).

In this work, these instrumental artifacts are included in the plots but omitted from the relevant discussions. Work is currently under

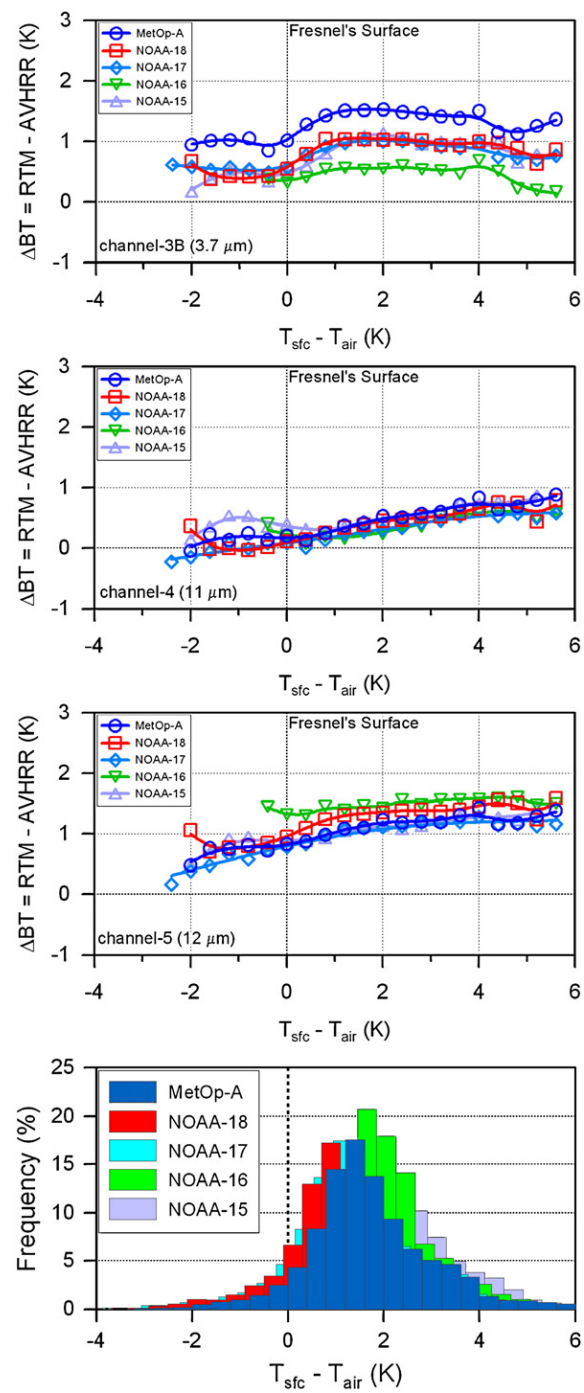

Fig. 10. Same as in Fig. 9 but as a function of the sea–air temperature difference (T_{sfc}−T_{air} binned at 0.4 K).

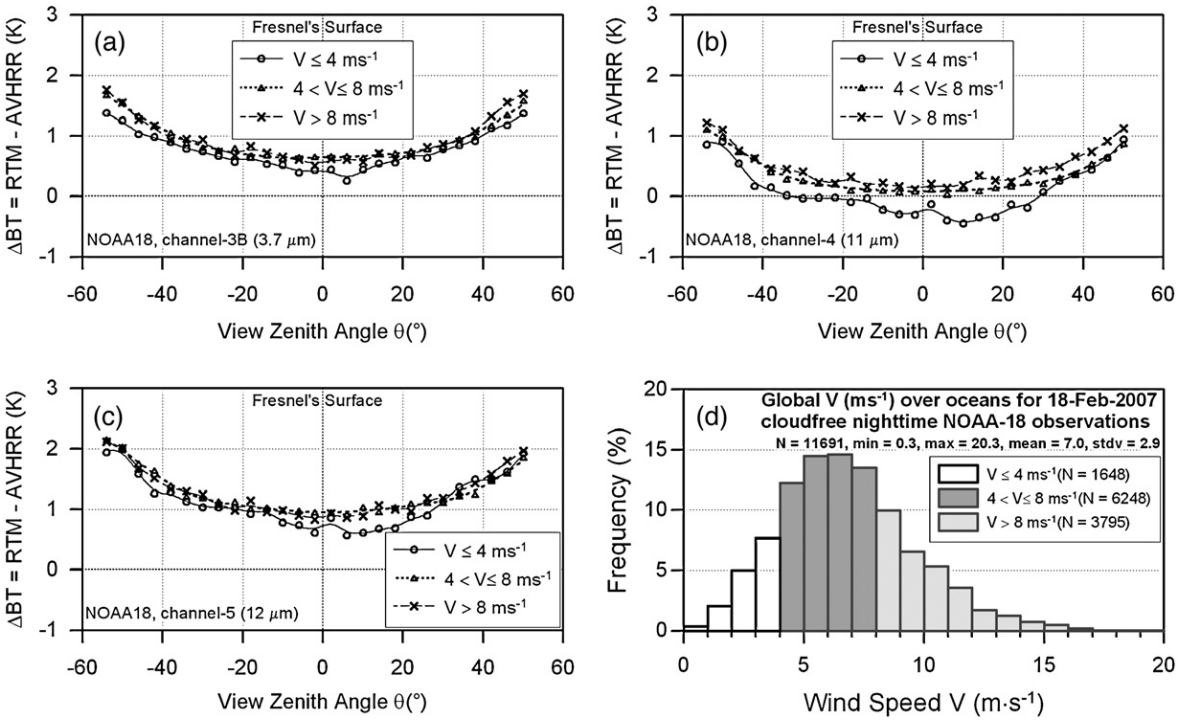

Fig. 11. Nighttime M−O biases for NOAA-18 as a function of view angle, θ, for low ($V \leq 4$ ms^{-1}), medium ($4 < V \leq 8$ ms^{-1}), and high ($V > 8$ ms^{-1}) wind speeds on 18 February 2007 in AVHRR channels (a) 3B, (b) 4, and (c) 5. (d) Histogram of near-surface wind speed with the three bins rendered in different shades (See discussion in Section 4.3).

way to explain and remove them from the data, and results of these analyses will be reported elsewhere.

4.2. View zenith angle dependence of the bias

Fig. 6 suggests that the M−O bias varies systematically across the swath. Fig. 8 checks this visual observation by plotting bias as a function of θ for all five platforms. All curves show remarkable cross-platform consistency. The agreement is best in channel 4, followed by channel 3B (except for NOAA-16 and MetOp-A as discussed above), and then by channel 5.

The RTM systematically underestimates the amplitude of angular dependence in TOA BTs compared to AVHRR. Increasing the amount of water vapor or trace gases in the atmosphere, or using a larger absorption coefficient in the RTM would reduce the magnitude of the bias. Also, this would flatten out its angular dependence because the effect of optical thickness on the BTs is approximately proportional to secθ. Including aerosols would have a similar effect on the TOA BTs as discussed below in Section 4.5.

For all angles, bias is considerably and consistently reduced for a Fresnel's surface, compared to a black surface. Similar Fresnel's-black surface comparison plots were generated for all remaining analyses in this section (not shown), and they invariably support this observation from Fig. 8. Hence, only Fresnel's results are shown and analyzed below in Figs. 9–12.

4.3. Geophysical dependence of the bias

Pronounced zonal trends in the M−O bias in Figs. 6 and 7 may be due to the global distribution of major geophysical parameters shown in Fig. 2. Fig. 9 shows the M−O bias as a function of W and T_{sfc}. Note that although W and T_{sfc} largely correlate on a global scale, the local correlation may break in certain areas such as in the tropics. Also, different AVHRR bands have different sensitivities to the atmosphere and surface.

The fact that the bias correlates more tightly with W than T_{sfc} in all bands suggests that it is likely due to the treatment of water vapor absorption in MODTRAN, in particular the CKD4.2 continuum formulation. Most noticeably, the bias structures in two longwave channels are similar but their magnitudes are offset by about ~0.65 K, despite the fact that these channels are spectrally close. Bias in channel 3B may be more sensitive to the unaccounted aerosol absorption (Table 5). Also recall that the Reynolds–Smith SST is likely biased warm at night as it is derived from both daytime and nighttime SST data, and channel 3B is the most sensitive band to any error in SST. However, the cause of the increasing trend in channel 3B M−O bias with increasing SST is not fully clear to us.

Fig. 10 shows that the bias tends to increase with increasing $T_{sfc}-T_{air}$. Ideally, the RTM should be able to work uniformly in the full range of environmental conditions, and existence of such trend signals a potential problem that should be addressed. For more analyses of sea air temperature difference on SST accuracy, readers are referred to May & Holyer (1993).

The surface emissivity model used in this study does not include effects of wind-induced roughness. The RTM is thus expected to perform best at low winds, when the surface is closest to the current assumptions, but may develop a progressive bias towards higher wind speeds. This bias, if it exists, should be more noticeable as one moves away from the nadir views. To check this hypothesis, Fig. 11 plots the M−O biases for NOAA-18 as a function of θ for three different wind speed (V) ranges: low ($V \leq 4$ ms^{-1}), medium ($4 < V \leq 8$ ms^{-1}), and high ($V > 8$ ms^{-1}).

For low wind speeds, the curves are quite noisy. This noise is mainly due to the fact that the correlation between bulk and skin SSTs (Section 2.1) breaks at low wind speeds (Donlon et al., 2002). It is further amplified by population size of the low-wind speed sample (approximately 15% of the total), which is much smaller than for the two other samples (~53% for medium and ~32% for high winds, respectively).

An important observation from Fig. 11 is that the RTM with a flat Fresnel's surface appears to perform uniformly in the full range of wind speeds. Based on their theoretical analyses, Watts et al. (1996) have concluded that for view zenith angles up to approximately 55°, the Fresnel's model is accurate to within 0.1 ± 0.1 K, at all wind speeds.

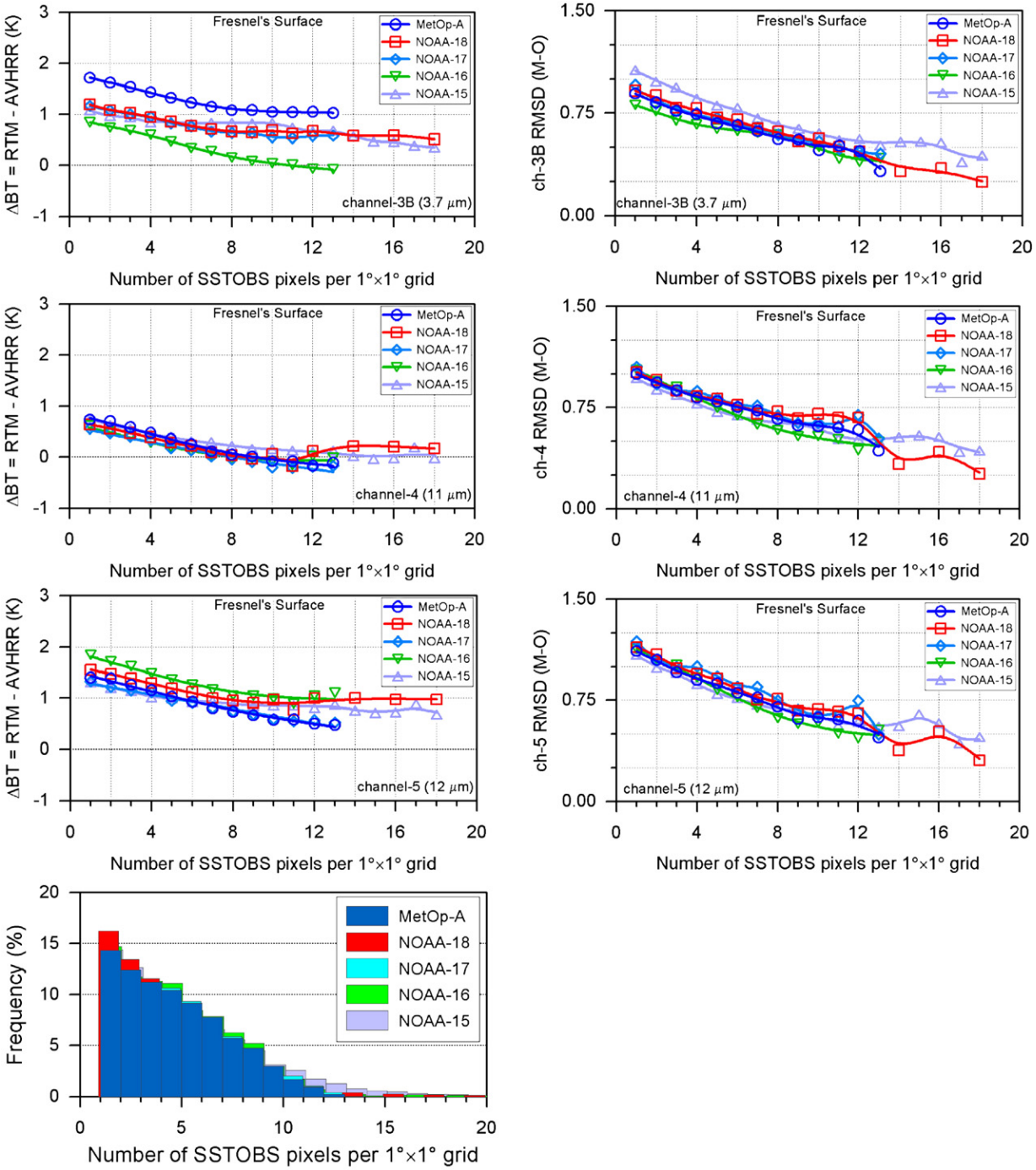

Fig. 12. (Left) Nighttime M−O biases and (right) RMSD versus number of observations (NOBS) within 1° grid-cells for three AVHRR channels onboard NOAA 15–18 and MetOp-A on 18 February 2007. Respective frequency distributions of NOBS are also shown (see discussion in Section 4.4).

This is due to the complex compensation mechanisms at higher wind speeds, between the decreased emissivity and increased downwelling atmospheric radiance (which is now coming from closer-to-horizon warmer atmospheric layers). Watts et al. concluded that the validity of these theoretical results needs to be confirmed by experiment. Similar conclusions were also drawn by Wu and Smith (1997), Hanafin and Minnett (2005), and Masuda (2006). Our data support these conclusions and provide additional evidence that adding wind speed effects to the current flat-surface emissivity model is unlikely to noticeably improve the TOA BTs, at least up to a zenith angle of 54° as tested in this study.

4.4. Effect of ambient and residual cloud on the M−O bias

The warm M−O bias may be due, at least in part, to a cold bias in the AVHRR BTs originating from the "indirect cloud effect". Although, clouds are removed from the data, they are often surrounded by areas of elevated humidity and aerosols (termed as "halos" in Perry and Hobbs, 1996). Such transient situations may go undetected by the threshold-based cloud masks and they are difficult to model. The halos have been known since at least 1949 as reviewed in Lu et al. (2003) and references therein. Furthermore, areas with elevated humidity and aerosols may be favored for cloud formation (Telford

and Wagner, 1980). Be it an elevated humidity, aerosols, or an unresolved sub-pixel cloud, the net effect of such transient situations is increase in the TOA visible reflectances and decrease in BTs. For instance, more recent analyses of aerosol retrievals from MODIS (Koren et al., 2007) and SEVIRI (De Paepe et al., 2008) have shown that the "aerosol halos" extend for tens of kilometers and may account for up to 30–60% of cloud-free population, depending upon threshold settings in different cloud masks.

We attempted to quantify the magnitude of this effect on the current validation results, using number of SSTOBS pixels within a 1° grid cell, NOBS as an approximate inverse proxy of ambient and residual cloud in the MUT data. (Note that the MUT system does not process every clear pixel and sampling patterns vary in space in time. Also, NOBS may be reduced in the coastal areas and near ice edges.) Fig. 12 shows that indeed, the mean M−O bias decreases as NOBS increases, for all channels and platforms, and it begins flattening out at NOBS ~8–10, suggesting that those 1° grid cells are likely confidently clear. According to Fig. 12, there are only 15–21% grid cells with NOBS≥8, but it is those pixels that are best suited to estimate the accuracy of the current RTM, which did not model this "indirect cloud effect". Note also that this cleanest sub-sample of the dataset is the most uniform within the 1° grid too, as attested by the reduced RMSD shown in the right column of Fig. 12.

Table 1 shows the mean biases and RMSDs of validation results using this cleanest subsample of only those grid cells with NOBS≥8. It is thus concluded that residual and ambient clouds do contribute to the M−O bias, but they cannot explain it all.

4.5. Effect of aerosols on the M−O bias

Table 1 shows that even if the cleanest AVHRR data are used, a warm M−O bias remains of approximately 0.67, 0.01 and 0.72 K in channels 3B, 4 and 5, respectively. It may be reduced if atmospheric aerosols are included in the RTM.

Review of the scientific literature suggests that at present, optical properties of various tropospheric and stratospheric aerosols in the thermal IR and their vertical distribution and effect on TOA BTs have not been sufficiently studied (e.g., Merchant et al., 1999; Highwood et al., 2003; Hollweg et al., 2006). Perangelo et al. (2004) suggest that in the absence of major volcanic eruptions, dust, being composed of coarse particles, is the major source of the TOA radiative forcing in the thermal IR. Despite the fact that the main focus in the aerosol analyses on the terrestrial radiation so far has been on mineral dust (Hollweg et al., 2006), "there is almost total lack of observations of optical properties of dust to date" (e.g., Highwood et al., 2003) and its vertical distribution remains highly uncertain (e.g., Merchant et al., 2006). Effects of other aerosols on the earth radiation are even less known.

Given this uncertainty, accurate quantification of the aerosol effect on the global M−O bias would require a considerable effort which is well beyond the scope of this work. As a quick estimate for dust-free oceanic conditions, optical depths of the "navy maritime" model aerosol in different AVHRR channels, and its effect on TOA BTs are shown in Tables 4 and 5, for nadir view. The effect on the TOA BTs is ~0.15 K in 3B, and ~0.07 K in channels 4 and 5, and it increases with the view zenith angle in proportion to $\sec\theta$. Based on the literature data, the "worst case scenario" estimates of the effect of dust on TOA BTs may reach several Kelvins at nadir (e.g., Sokolik, 2002; Highwood et al., 2003; Perangelo et al., 2004; Hollweg et al., 2006; Merchant et al., 2006). Considering that fraction of the global ocean covered with such extreme dust events is only a few percent, the effect on the global mean M−O biases in Table 1 is expected to be on the order of a few hundredths to tenths of a Kelvin.

More aerosol analyses are definitely needed. For these estimates to be realistic, aerosol fields should be specified from an established global model, e.g., GOCART (Chin et al., 2000). Work is currently underway to integrate global GOCART aerosol fields with the fast Community Radiative Transfer Model (CRTM; Kleespies et al., 2004; http://www.star.nesdis.noaa.gov/smcd/spb/CRTM/). Results of this effort will be reported elsewhere. However, "back-of-envelope" estimates given above in this section suggest that adding aerosols in the RTM would likely to keep the bias in channel 4 close to zero, to within a few tenths of a Kelvin, but it cannot reconcile the high biases in channels 3B and 5. Revisions to the MODTRAN4.2 spectroscopy are thus deemed needed (cf., Merchant et al., 1999).

5. Discussion and conclusion

In the past, several RTMs have been explored for analyses of SST retrievals (e.g., Barton et al., 1989; Zavody et al., 1995; Merchant et al., 1999; Kumar et al., 2003; Merchant & Le Borgne, 2004). An important step of validating RTM simulations against real satellite observations has been often omitted from these analyses. Our objective was to fill this void and check if the forward RTM based on MODTRAN4.2, used in conjunction with Fresnel's surface reflectance and global NCEP GDAS fields, can adequately reproduce the spectral, angular, and observational dependencies of the TOA radiances measured by the AVHRR sensors currently in orbit.

The RTM validation methodology adopted in this study is not fully new and has been partly tested with data from other sensors and for different applications (e.g., Garand, 2003; Uddstrom & McMillin, 1994; Morcrette, 1991). The focus of this study was to apply this methodology to test MODTRAN4.2 for SST applications. Also, we attempted to rule out the sensor uncertainty as the cause of the bias by doing analyses in three spectral bands of five AVHRRs onboard NOAA 15–18 and MetOp-A.

The major conclusion from our analyses is that the forward RTM does not reproduce AVHRR spectral, angular, and water vapor dependencies with accuracies acceptable for SST analyses. Coupling MODTRAN transmittances and upwelling and downwelling radiances with Fresnel's reflectance from a flat surface improves agreement between model and observations in all AVHRR bands. In agreement with the theoretical results by Watts et al. (1996), Wu and Smith (1997) and Masuda (2006), and with the empirical observations by Hanafin and Minnett (2005), our data also show that there is no evidence of significant wind speed dependence in the bias when a flat surface model is used. We thus conclude that including a wind-roughened surface emissivity model in the RTM is not expected to improve comparisons with AVHRR TOA BTs, at least up to a zenith angle of 54° as tested in this study. When a Fresnel's model is used, the M−O bias typically ranges from 0–2 K, depending upon band, view angle and atmospheric state. It is smallest in channel 4 and largest in channel 5, with channel 3B falling in between the two. In all bands, bias increases towards the edge of the scan.

The M−O bias is further reduced if one restricts the validation to only those AVHRR 1° grid cells that are most densely populated and in which the effect of ambient and residual cloud on AVHRR BTs is thus minimized. These effects have not been modeled in the current RTM. The average M−O biases in channels 3B, 4 and 5 in this "confidently clear-sky" sub-sample (from 12–17% of the total population) is 0.67, 0.01 and 0.72 K. Part of this remaining bias may come from large-scale regional bias in the NCEP GDAS global fields, and part from the aerosols which have not been included in the current analyses. In the future, we plan to repeat the current analyses with the European Centre for Medium-Range Weather Forecasts and with global aerosol fields, e.g., GOCART model. Preliminary estimates in this study suggest that this may reduce the biases but it will unlikely fully resolve all observed anomalies. Of particular concern is the large spectral inconsistency in biases between the spectrally close channels 4 and 5. This is thought to be mainly due to the treatment of water vapor absorption in

MODTARN4.2 using the outdated CKD2.4 water vapor continuum (Clough et al., 1989). Revisions to the current MODTRAN4.2 spectroscopy are necessary before it can be used for high-accuracy SST analyses and applications. This observation is largely consistent with the conclusions by Merchant et al. (1999). As of the time of this writing, MODTRAN5 model was announced. Once publicly available, it can be validated against AVHRR measurements in a way similar to the validation of MODTRAN4.2 in this study.

Results from all five sensors and platforms are very consistent, except for band 3B on two platforms, NOAA-16 and MetOp-A. The NOAA-16 anomaly is likely related to errors in its AVHRR spectral response functions. The source of the MetOp-A anomaly currently remains unclear. Note that there is also a similar "out-of-family" pattern in AVHRR channel 5 onboard NOAA-16 and -18, though of smaller magnitudes. Analyses are underway to understand and resolve all these sensor anomalies.

There is a wide range of real-time, global-scale applications, such as operational cloud masking, physical SST retrievals, and quality control of TOA BTs, for which MODTRAN in its current form is not well suited and for which fast RTM(s) should be used instead. The methodology described here can be easily adopted to validate any other RTM. In fact, validation of the NESDIS Community Radiative Transfer Model against AVHRR observations is currently underway using the approach described here, and its results will be reported elsewhere.

Acknowledgments

This work was supported by the Polar Product System Development and Implementation program managed by the NOAA/NESDIS Office of Systems Development, and by the Internal Government Studies managed by the NPOESS Integrated Program Office. P. Dash also acknowledges the CIRA visiting scientist fellowship for helping him to perform this research at NOAA/NESDIS. MODTRAN4.2 was made available from the US Air Force Research Laboratory, Hanscom AFB, Massachusetts, at a nominal fee. We thank John Sapper of NOAA/NESDIS OSDPD for a multi-year sustained effort to maintain the NESDIS MUT system and Jerry Sullivan of NOAA/NESDIS STAR for the helpful discussions related to AVHRR instrument. We appreciate the helpful discussions with Gail Anderson (NOAA) and Eric Shettle (Naval Research Laboratory), on MODTRAN. Finally, we thank anonymous reviewers for their constructive criticisms and helpful suggestions. The views, opinions, and findings contained in this report are those of the authors and should not be construed as an official NOAA or US Government position, policy, or decision.

Appendix A

Table 1A
Gaseous optical depths at nadir for channel 3B of five AVHRRs for six standard atmospheres calculated using MODTRAN4.2

Atmosphere	Species	MetOp-A	NOAA-18	NOAA-17	NOAA-16	NOAA-15
Tropical	Total	0.08917	0.08639	0.08774	0.09584	0.09065
	H_2O	0.05592	0.05063	0.05349	0.06329	0.06242
	H_2O continuum	0.01245	0.01224	0.01239	0.01386	0.01272
	CO_2+	0.01176	0.01137	0.01146	0.01111	0.00878
	O_3	0.00008	0.00009	0.00009	0.00011	0.00010
	N_2 continuum	0.00846	0.01150	0.00997	0.00813	0.00646
	Molecular scattering	0.00003	0.00002	0.00002	0.00002	0.00002
Mid-latitude summer	Total	0.07263	0.07128	0.07202	0.07796	0.07317
	H_2O	0.04453	0.04059	0.04285	0.05073	0.04999
	H_2O continuum	0.00773	0.00755	0.00767	0.00878	0.00795
	CO_2+	0.01138	0.01101	0.01110	0.01081	0.00849
	O_3	0.00010	0.00010	0.00011	0.00013	0.00012
	N_2 continuum	0.00850	0.01156	0.01002	0.00817	0.00649
	Molecular scattering	0.00003	0.00001	0.00002	0.00002	0.00002
Sub-arctic summer	Total	0.05973	0.05954	0.05977	0.06398	0.05951
	H_2O	0.03478	0.03194	0.03371	0.03996	0.03934
	H_2O continuum	0.00496	0.00483	0.00492	0.00573	0.00513
	CO_2+	0.01096	0.01057	0.01068	0.01056	0.00824
	O_3	0.00011	0.00011	0.00011	0.00014	0.00013
	N_2 continuum	0.00863	0.01173	0.01017	0.00829	0.00659
	Molecular scattering	0.00002	0.00001	0.00001	0.00002	0.00002
US standard 1976	Total	0.04952	0.05028	0.04998	0.05213	0.04792
	H_2O	0.02586	0.02388	0.02517	0.02989	0.02935
	H_2O continuum	0.00286	0.00275	0.00282	0.00339	0.00299
	CO_2+	0.01173	0.01137	0.01146	0.01105	0.00873
	O_3	0.00010	0.00011	0.00011	0.00013	0.00013
	N_2 continuum	0.00875	0.01190	0.01032	0.00840	0.00668
	Molecular scattering	0.00002	0.00001	0.00002	0.00002	0.00002
Mid-latitude winter	Total	0.03939	0.04113	0.04033	0.04065	0.03668
	H_2O	0.01691	0.01572	0.01658	0.01976	0.01934
	H_2O continuum	0.00165	0.00159	0.00163	0.00199	0.00174
	CO_2+	0.01150	0.01117	0.01126	0.01084	0.00853
	O_3	0.00012	0.00012	0.00013	0.00015	0.00014
	N_2 continuum	0.00909	0.01237	0.01072	0.00870	0.00694
	Molecular scattering	0.00003	0.00002	0.00002	0.00002	0.00002
Sub-arctic Winter	Total	0.03051	0.03298	0.03172	0.03036	0.02663
	H_2O	0.00888	0.00831	0.00877	0.01053	0.01023
	H_2O continuum	0.00070	0.00066	0.00068	0.00087	0.00074
	CO_2+	0.01147	0.01116	0.01124	0.01077	0.00847
	O_3	0.00012	0.00012	0.00013	0.00015	0.00014
	N_2 continuum	0.00930	0.01266	0.01097	0.00890	0.00710
	Molecular scattering	0.00002	0.00001	0.00002	0.00002	0.00002

Table 1B
The same as in Table 1A but for channel 4

Atmosphere	Species	MetOp-A	NOAA-18	NOAA-17	NOAA-16	NOAA-15
Tropical	Total	0.57698	0.57590	0.57449	0.59439	0.57787
	H_2O	0.03165	0.03420	0.03161	0.03142	0.03181
	H_2O continuum	0.53614	0.53221	0.53377	0.55451	0.53706
	CO_2+	0.00525	0.00561	0.00505	0.00427	0.00504
	O_3	0.00009	0.00013	0.00018	0.00010	0.00011
	TRACE	0.00059	0.00052	0.00057	0.00080	0.00060
	HNO_3	0.00050	0.00046	0.00048	0.00074	0.00052
Mid-latitude summer	Total	0.32645	0.32628	0.32509	0.33569	0.32692
	H_2O	0.02444	0.02614	0.02443	0.02422	0.02458
	H_2O continuum	0.29314	0.29098	0.29186	0.30338	0.29365
	CO_2+	0.00495	0.00528	0.00476	0.00402	0.00475
	O_3	0.00011	0.00016	0.00022	0.00012	0.00013
	TRACE	0.00058	0.00052	0.00056	0.00079	0.00059
	HNO_3	0.00049	0.00045	0.00047	0.00072	0.00051
Sub-arctic summer	Total	0.18643	0.18650	0.18568	0.19126	0.18667
	H_2O	0.01707	0.01811	0.01707	0.01682	0.01718
	H_2O continuum	0.16132	0.16011	0.16060	0.16709	0.16160
	CO_2+	0.00417	0.00446	0.00401	0.00338	0.00400
	O_3	0.00012	0.00017	0.00023	0.00013	0.00014
	TRACE	0.00056	0.00050	0.00055	0.00076	0.00057
	HNO_3	0.00047	0.00043	0.00045	0.00069	0.00049
US standard 1976	Total	0.09584	0.09623	0.09547	0.09764	0.09593
	H_2O	0.01315	0.01386	0.01315	0.01290	0.01324
	H_2O continuum	0.07494	0.07437	0.07460	0.07765	0.07507
	CO_2+	0.00394	0.00421	0.00378	0.00319	0.00377
	O_3	0.00009	0.00014	0.00019	0.00011	0.00011
	TRACE	0.00056	0.00050	0.00055	0.00076	0.00058
	HNO_3	0.00048	0.00043	0.00045	0.00069	0.00049
Mid-latitude winter	Total	0.04993	0.05022	0.04976	0.05048	0.04994
	H_2O	0.00750	0.00788	0.00750	0.00727	0.00755
	H_2O continuum	0.03541	0.03514	0.03525	0.03673	0.03548
	CO_2+	0.00322	0.00344	0.00309	0.00260	0.00308
	O_3	0.00009	0.00014	0.00019	0.00010	0.00011
	TRACE	0.00057	0.00050	0.00055	0.00077	0.00058
	HNO_3	0.00047	0.00043	0.00045	0.00069	0.00049
Sub-arctic winter	Total	0.01916	0.01937	0.01912	0.01898	0.01912
	H_2O	0.00322	0.00338	0.00322	0.00309	0.00324
	H_2O continuum	0.00970	0.00962	0.00965	0.01007	0.00971
	CO_2+	0.00247	0.00265	0.00237	0.00199	0.00236
	O_3	0.00008	0.00012	0.00017	0.00009	0.00010
	TRACE	0.00055	0.00048	0.00053	0.00074	0.00056
	HNO_3	0.00045	0.00041	0.00043	0.00066	0.00046

Table 1C
The same as in Table 1A but for channel 5

Atmosphere	Species	MetOp-A	NOAA-18	NOAA-17	NOAA-16	NOAA-15
Tropical	Total	0.80429	0.81970	0.79269	0.80965	0.79409
	H_2O	0.01123	0.01086	0.00970	0.01112	0.01128
	H_2O continuum	0.78588	0.80046	0.77635	0.79032	0.77608
	CO_2+	0.00377	0.00455	0.00311	0.00416	0.00302
	O_3	0.00007	0.00007	0.00004	0.00008	0.00004
	TRACE	0.00016	0.00012	0.00018	0.00013	0.00020
	HNO_3	0.00013	0.00008	0.00014	0.00009	0.00016
Mid-latitude summer	Total	0.44604	0.45500	0.43912	0.44948	0.44008
	H_2O	0.00765	0.00740	0.00659	0.00755	0.00766
	H_2O continuum	0.43135	0.43949	0.42600	0.43393	0.42584
	CO_2+	0.00357	0.00431	0.00293	0.00395	0.00284
	O_3	0.00009	0.00008	0.00005	0.00010	0.00005
	TRACE	0.00017	0.00012	0.00018	0.00013	0.00020
	HNO_3	0.00013	0.00009	0.00014	0.00009	0.00016
Sub-arctic summer	Total	0.24980	0.25515	0.24566	0.25211	0.24624
	H_2O	0.00439	0.00424	0.00371	0.00429	0.00435
	H_2O continuum	0.23886	0.24344	0.23584	0.24034	0.23575
	CO_2+	0.00304	0.00367	0.00247	0.00339	0.00239
	O_3	0.00009	0.00009	0.00006	0.00010	0.00006
	TRACE	0.00016	0.00012	0.00018	0.00013	0.00019
	HNO_3	0.00012	0.00008	0.00014	0.00009	0.00015
US standard 1976	Total	0.12104	0.12398	0.11870	0.12260	0.11909
	H_2O	0.00302	0.00291	0.00256	0.00294	0.00297
	H_2O continuum	0.11157	0.11377	0.11012	0.11230	0.11007
	CO_2+	0.00289	0.00348	0.00234	0.00321	0.00226
	O_3	0.00008	0.00008	0.00005	0.00010	0.00005

Table 1C (continued)

Atmosphere	Species	MetOp-A	NOAA-18	NOAA-17	NOAA-16	NOAA-15
US standard 1976	TRACE	0.00016	0.00012	0.00017	0.00012	0.00019
	HNO_3	0.00012	0.00008	0.00014	0.00009	0.00015
Mid-latitude winter	Total	0.06060	0.06236	0.05929	0.06178	0.05948
	H_2O	0.00136	0.00130	0.00112	0.00130	0.00131
	H_2O continuum	0.05324	0.05432	0.05252	0.05360	0.05250
	CO_2+	0.00241	0.00290	0.00193	0.00270	0.00186
	O_3	0.00009	0.00008	0.00005	0.00010	0.00005
	TRACE	0.00016	0.00012	0.00017	0.00012	0.00019
	HNO_3	0.00012	0.00008	0.00013	0.00009	0.00015
Sub-arctic winter	Total	0.02085	0.02176	0.02024	0.02177	0.02033
	H_2O	0.00046	0.00044	0.00037	0.00044	0.00043
	H_2O continuum	0.01490	0.01522	0.01468	0.01501	0.01467
	CO_2+	0.00191	0.00228	0.00149	0.00215	0.00144
	O_3	0.00008	0.00008	0.00005	0.00010	0.00005
	TRACE	0.00016	0.00011	0.00017	0.00012	0.00019
	HNO_3	0.00011	0.00008	0.00013	0.00008	0.00014

Table 2
Column-integrated amounts of absorbing gases in six standard atmospheres. Unit conversion:1 atm-cm = M/(2.24×10^4) 1 g/cm^2, where M = molecular weight. (M: H_2O = 18.016, O_3 = 48, CO_2 = 44.01, CO = 28.01, CH_4 = 16.042, N_2O = 16.042, NH_3 = 17.034, NO = 30.010, NO_2 = 46.01, SO_2 = 64.065, HNO_3 = 63.018)

Species (g cm^{-2})	Tropical	Mid-latitude summer	Sub-arctic summer	US standard 1976	Mid-latitude winter	Sub-arctic winter
H_2 O (E+0)	4.122	2.926	2.081	1.418	0.852	0.416
O_3 (E−4)	5.953	7.116	7.397	7.365	8.083	8.052
CO_2 (E−1)	5.697	5.677	5.651	5.665	5.693	5.664
CO (E−4)	1.096	1.097	1.100	1.110	1.126	1.137
CH_4 (E−4)	9.480	9.089	8.992	9.454	9.165	9.108
N_2O (E−4)	1.764	1.700	1.571	1.760	1.722	1.719
NH_3 (E−7)	1.292	1.302	1.323	1.332	1.372	1.400
NO (E−7)	4.252	4.330	4.325	4.211	4.152	4.057
NO_2 (E−7)	4.336	4.487	4.433	4.201	4.081	3.838
SO_2 (E−7)	3.087	3.099	3.125	3.146	3.216	3.258
HNO_3 (E−6)	1.071	1.079	1.054	1.022	1.003	0.953
Species (atm cm)						
H_2O (E+3)	5.125	3.638	2.588	1.763	1.060	0.518
O_3 (E−1)	2.778	3.321	3.452	3.437	3.772	3.758
CO_2 (E+2)	2.899	2.889	2.876	2.883	2.897	2.883
CO (E−2)	8.768	8.776	8.799	8.876	9.002	9.095
CH_4 (E+0)	1.324	1.269	1.256	1.320	1.280	1.272
N_2O (E−1)	2.463	2.374	2.194	2.457	2.405	2.400
NH_3 (E−4)	1.698	1.712	1.739	1.752	1.804	1.842
NO (E−4)	3.173	3.232	3.228	3.143	3.099	3.028
NO_2 (E−4)	2.111	2.184	2.158	2.045	1.987	1.868
SO_2 (E−4)	1.079	1.084	1.093	1.100	1.124	1.139
HNO_3 (E−4)	3.806	3.835	3.747	3.634	3.565	3.388

Table 3
Effect of trace gases on TOA BTs for three AVHRR channels onboard five platforms and for six standard atmospheres (partial derivatives are calculated as BT differences for simulations without and with all mid-latitude summer trace gases)

AVHRR/platform	Standard atmosphere	Ch-3B ΔBT	Ch-4 ΔBT	Ch-5 ΔBT
MetOp-A	Tropical	0.2008	0.0870	0.0868
	Mid-latitude summer	0.1787	0.0826	0.0825
	Sub-arctic summer	0.1655	0.0796	0.0792
	US standard 1976	0.1938	0.0883	0.0897
	Mid-latitude winter	0.1491	0.0674	0.0682
	Sub-arctic winter	0.1096	0.0488	0.0493
NOAA-18	Tropical	0.1981	0.0880	0.0865
	Mid-latitude summer	0.1763	0.0838	0.0823
	Sub-arctic summer	0.1628	0.0807	0.0790
	US standard 1976	0.1913	0.0895	0.0894
	Mid-latitude winter	0.1472	0.0684	0.0678
	Sub-arctic winter	0.1081	0.0496	0.0490
NOAA-17	Tropical	0.1956	0.0908	0.0897
	Mid-latitude summer	0.1741	0.0870	0.0851
	Sub-arctic summer	0.1610	0.0838	0.0817
	US standard 1976	0.1891	0.0925	0.0926
	Mid-latitude winter	0.1457	0.0709	0.0700
	Sub-arctic winter	0.1072	0.0513	0.0505
NOAA-16	Tropical	0.1410	0.0833	0.0962
	Mid-latitude summer	0.1260	0.0792	0.0916
	Sub-arctic summer	0.1182	0.0762	0.0880
	US standard 1976	0.1358	0.0847	0.0998

(*continued on next page*)

Table 3 (continued)

AVHRR/platform	Standard atmosphere	Ch-3B ΔBT	Ch-4 ΔBT	Ch-5 ΔBT
NOAA-16	Mid-latitude winter	0.1049	0.0647	0.0759
	Sub-arctic winter	0.0775	0.0467	0.0550
NOAA-15	Tropical	0.1333	0.0875	0.0918
	Mid-latitude summer	0.1185	0.0831	0.0870
	Sub-arctic summer	0.1108	0.0801	0.0836
	US standard 1976	0.1280	0.0890	0.0946
	Mid-latitude winter	0.0976	0.0679	0.0716
	Sub-arctic winter	0.0708	0.0491	0.0517

Table 4
Aerosol Optical Depths (AOD) of Navy Maritime aerosol model for three AVHRR channels onboard MetOp-A for standard atmospheres in spring–summer season

Standard atmosphere	*V*	RH	*M*	Navy Maritime Aerosol Optical Depth (×10^3), spring–summer					
				Ch3B		Ch4		Ch5	
				Total	Absorption	Total	Absorption	Total	Absorption
Tropical	4.10	75.59	101.58	21.84	2.13	7.85	4.41	8.53	6.18
Mid-latitude summer	4.10	76.18	100.92	22.12	2.15	7.93	4.47	8.63	6.26
Sub-arctic summer	6.69	75.23	56.73	45.57	3.39	13.87	7.95	15.89	11.88
US standard 1976	7.20	50.00	77.29	25.29	2.25	8.71	4.51	9.14	6.32
Mid-latitude winter	10.29	77.07	33.98	83.82	5.54	24.35	14.02	28.50	21.47

The values for Fall–Winter season and for other four AVHRRs (not shown) are comparable to within 3 significant digits after decimal point. Default MODTRAN4.2 values of near-surface wind speed, RH, and meteorological range (M) used in aerosol calculations are also shown.
V = average 24h wind speed (m/s), RH = relative humidity (%), *M* = meteorological range (km).

Table 5
The same as in Table 3 but for TOA BT difference ("without aerosol minus with aerosol")

AVHRR Platform	Standard atmosphere	Navy maritime model aerosol, spring–summer		
		Ch3B ΔBT	Ch4 ΔBT	Ch5 ΔBT
MetOp-A	Tropical	0.129	0.076	0.043
	Mid-latitude summer	0.108	0.066	0.045
	Sub-arctic summer	0.235	0.101	0.092
	US standard 1976	0.156	0.085	0.073
	Mid-latitude winter	0.284	0.110	0.117

References

Anderson, G. P., Berk, A., Chetwynd, J. H., Harder, G., Fontenla, J. M., Shettle, E. P., et al. (2007). Using the MODTRAN™5 radiative transfer algorithm with NASA satellite data: AIRS and SORCE. In S. S. Shen, & P. E. Lewis (Eds.), *Proceedings of SPIE, Algorithms and Technologies for Multispectral, Hyperspectral, and Ultraspectral Imagery XIII, vol. 6565*. doi:10.1117/12.721184

Barton, I. J., Zavody, A. M., O'Brien, D. M., Cutten, D. R., Saunders, R. W., & Llewelyn-Jones, D. T. (1989). Theoretical algorithms for satellite-derived sea surface temperatures. *Journal of Geophysical Research*, *94*, 3365–3375.

Berk, A., Anderson, G. P., Acharya, P. K., Chetwynd, J. H., Bernstein, L. S., Shettle, E. P., et al. (2000, Apr. 17). MODTRAN4 v2 User's Manual, Air Force Research Laboratory, Space Vehicles Directorate, Hanscom AFB, MA, USA.

Berk, A., Bernstein, L. S., Anderson, G. P., Acharya, P. K., Robertson, D. C., Chetwynd, J. H., et al. (1998). MODTRAN cloud and multiple scattering upgrades with application to AVIRIS. *Remote Sensing of Environment*, *65*, 367–375.

Brown, O. B., & Minnett, P. J. (1999, Apr. 30). *MODIS Infrared Sea Surface Temperature Algorithm, Algorithm Theoretical Basis Document, v2.0.*Miami, FL: University of Miami 33149–1098 (available at: http://modis.gsfc.nasa.gov/data/atbd/ocean_atbd.php).

Cao, C., Weinreb, M., & Sullivan, J. (2001). Solar contamination effects on the infrared channels of the advanced very high resolution radiometer. *Journal of Geophysical Research*, *106*, 33463–33469.

Chin, M., Rood, R. B., Lin, S. -J., Muller, J. F., & Thomspon, A. M. (2000). Atmospheric sulfur cycle in the global model GOCART: Model description and global properties. *Journal of Geophysical Research*, *105*, 24671–24687.

Clough, S. A., Kneizys, F. X., & Davies, R. W. (1989). Line shape and water vapor continuum. *Atmospheric Research*, *23*, 229–241.

De Paepe, B., Ignatov, A., Dewitte, S., & Ipe, A. (2008). Aerosol retrievals over ocean from SEVIRI for the use in GERB Earth's Radiation Budget Analyses. *Remote Sensing of Environment*, *112*, 2455–2468.

Deschamps, P. Y., & Phulpin, T. (1980). Atmospheric correction of infrared measurements of sea surface temperature using channels at 3.7, 11 and 12 μm. *Boundary-Layer Meteorology*, *18*, 131–143.

Donlon, C. J., Minnett, P. J., Gentlemann, T. J., Barton, I. J., Ward, B., & Murray, M. J. (2002). Toward improved validation of satellite surface skin temperature measurements for climate research. *Journal of Climate*, *15*, 353–369.

Downing, H. D., & Williams, D. (1975). Optical constants of water in the infrared. *Journal of Geophysical Research*, *80*, 1656–1661.

Francois, C., Brisson, A., Le Borgne, P., & Marsouin, A. (2002). Definition of a radiosounding database for sea surface brightness temperature simulations: Application to sea surface temperature retrieval algorithm determination. *Remote Sensing of Environment*, *81*, 309–326.

Friedman, D. (1969). Infrared characteristics of ocean water (1.5–15 μm). *Applied Optics*, *8*, 2073–2078.

Garand, L. (2003). Toward an integrated land–ocean surface skin temperature analysis from the variational assimilation of infrared radiances. *Journal of Applied Meteorology*, *42*, 570–583.

Goodrum, G., Kidwell, K., & Winston, W. (Eds.). (2003). *NOAA-KLM user's guide with NOAA-N, -N' supplement. NOAA/NESDIS, Available from National Climatic Data Center, 151 Patton Ave., Asheville, NC 28801-5001* (Also available from: http://www2.ncdc.noaa.gov/docs/klm/index.htm).

Hale, G. M., & Querry, M. R. (1973). Optical constants of water in the 200-nm to 200-μm wavelength region. *Applied Optics*, *12*, 555–563.

Hanafin, J. A., & Minnett, P. J. (2005). Measurements of the infrared emissivity of a wind-roughened sea surface. *Applied Optics*, *44*(3), 398–411.

Highwood, E. J., Haywood, J. M., Silverstone, M. D., Newman, S. M., & Taylor, J. P. (2003). Radiative properties and direct effect of Saharan dust measured by the C-130 aircraft during Saharan Dust Experiment (SHADE): 2. Terrestrial spectrum. *Journal of Geophysical Research*, *108*. doi:10.1029/2002JD002552

Hollweg, H. -D., Bakan, S., & Taylor, J. P. (2006). Is the aerosol emission detectable in the thermal infrared? *Journal of Geophysical Research*, *111*, 1–13. doi:10.1029/2005JD006432, D15202

Ignatov, A., Sapper, J., Laszlo, I., Nalli, N., Harris, A., Pichel, W., et al. (2004). *Global operational sea surface temperature and aerosol products from AVHRR: Current status, diagnostics, and potential enhancements*. 13th AMS Conference on Satellite Oceanography and Meteorology, Norfolk, Virginia, 20–24 September.

ITT (2007). *Advanced Very High Resolution Radiometer/3, instruction manual and alignment/calibration handbook (SN A305). Contract NAS5-30384.*Fort Wayne, IN: ITT Aerospace/Communications Division 411 pp.

Kleespies, T. J., van Delst, P., McMillin, L. M., & Derber, J. (2004). Atmospheric transmittance and an absorbing gas. 6. OPTRAN status report and introduction to the NESDIS/NCEP Community Radiative Transfer Model. *Applied Optics, 43*, *15*, 3103–3109.

Koren, I., Remer, L. A., Kaufman, Y. J., Rudich, Y., & Martins, J. V. (2007). On the twilight zone between clouds and aerosols. *Geophysical Research Letters*, *34*. doi:10.1029/2007GL029253

Kumar, A., Minnett, P. J., Podesta, G., & Evans, R. E. (2003). Error characteristics of the atmospheric correction algorithms used in retrieval of sea surface temperatures from infrared satellite measurements: Global and regional aspects. *Journal of Atmospheric Sciences*, *60*, 575–585.

Lu, M. -L., Wang, J., Freedman, A., Jonsson, H. H., Flagan, R. C., McClatchey, R. A., et al. (2003). Analysis of humidity halos around trade wind cumulus clouds. *Journal of the Atmospheric Sciences*, *60*, 1041–1059.

May, D. A., & Holyer, R. J. (1993). Sensitivity of satellite multichannel sea surface temperature retrievals to the air–sea temperature difference. *Journal of Geophysical Research*, *98*, 12567–12578.

Masuda, K. (2006). Infrared sea surface emissivity including multiple reflection effect for isotropic Gaussian slope distribution model. *Remote Sensing of Environment*, *103*, 488–496.

Masuda, K., Takashima, T., & Takayama, Y. (1988). Emissivity for pure and sea water for the model sea surface in the infrared window regions. *Remote Sensing of Environment*, *24*, 313–329.

McClain, E. P., Pichel, W. G., & Walton, C. C. (1985). Comparative performance of AVHRR-based multichannel sea surface temperatures. *Journal of Geophysical Research*, *90*, 11587–11601.

Merchant, C. J., Embury, O., Le Borgne, P., & Bellec, B. (2006). Saharan dust in nighttime thermal imagery: Detection and reduction of related biases in retrieved sea surface temperature. *Remote Sensing of Environment*, *104*, 15–30.

Merchant, C. J., Harris, A. R., Murray, M. J., & Zavody, A. M. (1999). Towards the elimination of bias in satellite retrievals of sea surface temperatures, 1. Theory, modeling and interalgorithm comparison. *Journal of Geophysical Research*, *104*, 23565–23578.

Merchant, C. J., & Le Borgne, P. (2004). Retrieval of sea surface temperature from space, based on modeling of infrared radiative transfer: Capabilities and limitations. *Journal of Atmospheric and Oceanic Technology*, *21*, 1734–1746.

Morcrette, J. J. (1991). Evaluation of model-generated cloudiness: Satellite-derived and mode-generated diurnal variability of brightness temperature. *Monthly Weather Review*, *119*, 1205–1224.

Newman, S. M., Smith, J. A., Glew, M. D., Rogers, S. M., & Taylor, J. P. (2005). Temperature and salinity dependence of sea surface emissivity in the thermal infrared. *Quarterly Journal of the Royal Meteorological Society*, *131*, 2539–2557.

Perry, K. D., & Hobbs, P. V. (1996). Influences of isolated cumulus clouds on the humidity of their surroundings. *Journal of Atmospheric Sciences*, *53*, 159–174.

Perangelo, C., Chedin, A., Heilliette, S., Jacquinet-Husson, N., & Armante, R. (2004). Dust altitude and infrared optical depth from AIRS. *Atmospheric Chemistry and Physics*, *4*, 1813–1822.

Pinkley, L. W., Sethna, P. P., & Williams, D. (1977). Optical constants of water in the infrared: Influence of temperature. *Journal of Optical Society of America*, *678*, 494–499.

Reynolds, R. W., Rayner, N. A., Smith, T. M., Stokes, D. C., & Wang, W. (2002). An improved in situ and satellite SST analysis for climate. *Journal of Climate*, *15*, 1609–1625.

Rothman, L. S., Barbie, A., Benner, D. C., Brown, L. R., Cammy-Peyret, C., Carleer, M. R., et al. (2003). The HITRAN molecular spectroscopic database: Edition of 2000 including updates through 2001. *Journal of Quantitative Spectroscopy and Radiative Transfer*, *82*, 5–44.

Saunders, R., Rayer, P., Brunel, P., von Engeln, A., et al. (2007). A comparison of radiative transfer models for simulating Atmospheric Infrared Sounder (AIRS) radiance. *Journal of Geophysical Research*, *112*, D01S90. doi:10.1029/2006JD007088

Segelstein, D.J. (1981). The complex refractive index of water. M.S. thesis. University of Missouri, Kansas City, MO.

Sikorski, R. J., Miller, S. W., & Kealy, P. S. (2002, March). *Sea Surface Temperature, Visible and Infrared Imager/Radiometer Suite, Algorithm Theoretical Basis Document, v5.0, Raytheon Systems Company.* (available at: http://npoesslib.ipo.noaa.gov).

Smith, W. L., Knuteson, R. O., Revercomb, H. E., Feltz, W., Howell, H. B., Menzel, W. P., et al. (1996). Observations of the infrared radiative properties of the ocean — Implications for the measurement of sea surface temperature via satellite remote sensing. *Bulletin of the American Meteorological Society*, *77*, 41–51.

Sokolik, I. (2002). The spectral radiative signature of wind-blown mineral dust: Implications for remote sensing in the thermal IR region. *Geophysical Research Letters*, *29*(24). doi:10.1029/2002GL015910

Steyn-Ross, D. A., Steyn-Ross, M. L., & Clift, S. (1992). Radiance calibrations for Advanced Very High Resolution Radiometer infrared channels. *Journal of Geophysical Research*, *97*, 5551–5568.

Susskind, J., Rosenfield, J., Reuter, D., & Chahine, M. (1984). Remote sensing of weather and climate parameters from HIRS/2 MSU on Tiros-N. *Journal of Geophysical Research*, *89*(D3), 4677–4697.

Telford, J. W., & Wagner, P. B. (1980). The dynamical and liquid water structure of the small cumulus as determined from its environment. *Pure and Applied. Geophysics*, *118*, 935–952.

Uddstrom, M. J., & McMillin, L. M. (1994). System noise in the NESDIS TOVS forward model. Part I: Specification. *Journal of Applied Meteorology*, *33*, 919–938.

Walton, C. C., Pichel, W. G., Sapper, J. F., & May, D. (1998). The development and operational applications of nonlinear algorithms for the measurement of sea surface temperatures with the NOAA polar-orbiting environmental satellites. *Journal of Geophysical Research*, *103*, 27999–28012.

Watts, P. D., Allen, M. R., & Nightingale, T. J. (1996). Wind speed effects on sea surface emission and reflection for the Along Track Scanning Radiometer. *Journal of Atmospheric and Oceanic Technology*, *13*, 126–141.

Wu, X., & Smith, W. L. (1997). Emissivity of rough sea surface for 8–13 μm: Modeling and verification. *Applied Optics*, *36*, 2609–2619.

World Meteorological Organization (WMO) (1986). *World Climate Programme (WCP)-112, A preliminary cloudless standard atmosphere for radiation computation.* World Meteorological Organization, WMO/TD-No. 24, Geneva, Switzerland.

Zavody, A. M., Mutlow, C. T., & Llewelyn-Jones, D. T. (1995). A radiative transfer model for sea surface temperature retrieval for the along-track scanning radiometer. *Journal of Geophysical Research*, *100*, 937–952.